POLYTECHNIQUE MONTRÉAL
affiliée à l'Université de Montréal

Foundation for Singlet Delta Oxygen Production Optimization by Atmospheric Pressure He/O_2 plasmas

JEAN-PHILIPPE COMTOIS
Département de génie physique

Mémoire présenté en vue de l'obtention du diplôme de *Maîtrise* ès *sciences appliquées*
Génie physique

Août 2025

© Jean-Philippe Comtois, 2025.

POLYTECHNIQUE MONTRÉAL
affiliée à l'Université de Montréal

Ce mémoire intitulé :

Foundation for Singlet Delta Oxygen Production Optimization by Atmospheric Pressure He/O_2 plasmas

présenté par **Jean-Philippe COMTOIS**
en vue de l'obtention du diplôme de *Maîtrise* ès *sciences appliquées*
a été dûment accepté par le jury d'examen constitué de :

Ludvik MARTINU, président
Stephan REUTER, membre et directeur de recherche
Frédéric SIROIS, membre et codirecteur de recherche
Denis SELETSKIY, membre

DEDICATION

To all my friends and family,
Thank you...

ACKNOWLEDGEMENTS

I would like to first thank my supervisor Pr. Stephan Reuter and my co-supervisor Pr. Frédéric Sirois for their invaluable guidance throughout this process. Special thanks to all the lab members: Sean Watson, Jean-Baptiste Billeau, Julien Trahan, Laura Bouret, Juliette Letellier-Bao, Nathan Sasseville-Langelier, Roxanne Thomas, Laura Cacot and David Brassard for all the fruitful discussions and advices. Many thanks to Joël Bouchard and Yanik Landry-Ducharme for their technical expertise and insights. I am sincerely thankful to my father, my mother, my sister, and my friends for their continuous support of my studies. Finally, I would like to acknowledge Polytechnique Montréal for the financial support and the opportunity to carry out this work.

RÉSUMÉ

Ce mémoire pose les fondations vers l'obtention d'un meilleur contrôle sur la production des espèces chimiques réactives produites par les plasmas hors-équilibre à pression atmosphérique, avec une attention particulière à l'oxygène delta singulet produit par un jet de plasma He/O_2 couplé capacitivement. Un contrôle sur la production de ces espèces est ici défini par un champ électrique impulsionnel modifiable, une détection sensible des espèces, puis l'établissement d'un modèle permettant de simuler et de comprendre les mécanismes de formation et de destruction de celles-ci.
Afin d'atteindre une production maximale d'oxygène delta singulet, une excitation électrique radio-fréquence combinée avec des pulses haute tension d'une durée de quelques nanosecondes est envisagée. Ainsi, la création d'une source pulsée haute tension est une partie importante de ce travail. Cette source est basée sur un générateur de type Cockcroft-Walton qui produit une haute tension DC. Cette haute tension est ensuite commutée par un interrupteur commercial haute tension basé sur la technologie MOSFET. L'interrupteur est actionné par un circuit de contrôle maison. Cette source pulsée haute tension a allumé un plasma dans l'air avec succès à l'aide d'un réacteur de décharges à barrière diélectrique de test. Les caractéristiques typiques du pulse produisant le plasma sont une amplitude de 6 kV, une fréquence de répétition de 2 kHz, une largeur à mi-hauteur de 1 μs avec un temps de montée de 40 ns. L'étendu des performances de la source sont une amplitude allant de 0 à 8 kV, une fréquence de répétition de 500 Hz à 8 kHz, une largeur à mi-hauteur de 1 μs à 10 μs.

Un système de spectroscopie dans le proche infrarouge est recréé afin de mesurer des densités absolues d'oxygène delta singulet dans l'effluent d'un jet de plasma à pression atmosphérique. L'effluent est acheminé par un tube de verre vers une cellule de détection calibrée. Certains des photons émis dans cette cellule passent par un filtre passe-bande puis atteignent une photodiode InGaAs. La tension mesurée par cette photodiode est associé à une densité absolue d'oxygène singulet par un facteur de conversion obtenu de la littérature. La densité maximale mesurée d'oxygène delta singulet est $1.1 * 10^{15}$ molécules/cm^3 et est obtenue pour un plasma de 35 W, ayant une fréquence d'excitation de 13.56 MHz, une composition gazeuse de 0.998 : 0.002 (He : O2) avec un flux total de 14 SLM à une distance de détection de 14 cm. La limite de détection est posée à 10^{14} molécules/cm^3. Un système de détection d'ozone est utilisé dans l'effluent du même jet de plasma à pression atmosphérique pour l'importance de cette molécule dans les mécanismes de destruction de l'oxygène delta singulet. Avec la loi de Beer-Lambert et les spectres enregistrés à l'aide d'un spectromètre suite à l'absorption

UV, notamment à 254 nm, dans une cellule de détection, des densités absolue d'ozone sont obtenues.

La cinétique du plasma est modélisé en incorporant un solveur d'équation de Boltzmann dépendant du temps (Loki-B) dans un outil maison MATLAB permettant de résoudre l'évolution des densités d'espèces chimiques dans le temps. L'utilisation d'un solveur d'équation de Boltzmann dépendant du temps est essentiel lorsque qu'un champ d'excitation électrique nano-pulsé est utilisé. Puisque qu'une telle excitation est envisagée et qu'aucun solveur existant dépendant du temps ne possède une architecture supportant les réactions chimiques, la création d'un tel modèle global était nécessaire. Cet outil, qui contient une interface graphique pour la facilité d'utilisation, est comparé à un outil déjà établi, soit ZDPlasKin, en recréant deux de ses exemples. Les résultants sont extrêmement similaires et confirme une comparaison réussie. Ensuite, un modèle de mélange gazeux He : O_2 est choisi dans la littérature afin de simuler les résultats expérimentaux à température et pression ambiante et une puissance de 35 W. Toutefois, les résultats de ce modèle complexe de 120 réactions chimiques ne n'atteignent pas l'équilibre.
En somme, ce mémoire établi la fondation pour la création d'une source de puissance nano-pulsée combinée avec une excitation radio-fréquence alimentant un plasma à pression atmosphérique He :O_2, la détection d'oxygène delta singulet dans son effluent et la création d'un modèle global cinétique permettant de suivre l'évolution de la densité des espèces chimique compatible avec l'excitation électrique voulue. Ces avancées permettent une progression vers un meilleur contrôle des espèces chimiques réactives produites par les plasmas hors-équilibre à pression atmosphérique.

ABSTRACT

This work lays the foundation for better control over the produced reactive species by non-thermal (NT) plasmas at atmospheric pressure, with a main focus on singlet delta oxygen ($O_2(^1\Delta_g)$) generated by a capacitively coupled He/O_2 plasma jet for its relevance in biomedicine, agriculture and plasma-assisted combustion. This work provides the tools to control, understand, and monitor the $O_2(^1\Delta_g)$ production by the means of a modifiable electric field, a sensitive measurement of $O_2(^1\Delta_g)$, and a kinetic model.

To achieve maximum $O_2(^1\Delta_g)$ generation, a nano-second (ns)-pulse combined with RF electrical excitation is planned, so a core part of the thesis is the construction of a pulse high voltage power supply. The electric pulser is based on a Cockcroft-Walton (CW) generator which creates a high voltage DC that is switched on by a solid-state high voltage switch triggered by an in-house control circuit. The pulser successfully ignited a dielectric barrier discharge reactor with pulse characteristics around 6 kV in amplitude, 2 kHz repetition frequency, 1 μs full width half maximum (FWHM) and 40 ns rise time. The full range of the pulser goes from 0 to 8 kV in amplitude, 500 Hz to 8 kHz repetition frequency, 1 to 10 μs FWHM.

A near infrared (NIR) emission spectroscopy at 1270 nm setup is recreated to measure the absolute densities of $O_2(^1\Delta_g)$ in the effluent of an atmospheric pressure plasma jet (APPJ). The effluent is collected by a glass adapter and redirected to a calibrated cell. Photons pass through a narrow bandpass filter before reaching an InGaAs photodiode. The measured voltage is converted to an absolute density by a conversion factor obtained from literature. The maximum measured density of $O_2(^1\Delta_g)$ is $1.1 * 10^{15}$ molecules/cm^3 and obtained in the effluent of a 35 W, 13.56 MHz, He:O2 (0.998:0.002) plasma at 14 cm detection distance where the total gas flow is 14 SLM. The detection limit is set at 10^{14} molecules/cm^3. For its relevance in $O_2(^1\Delta_g)$ quenching mechanisms, an ozone detection setup is also used in the effluent of this jet. Absorption signals are obtained by a spectrometer and from ultra-violet (UV) absorption at 254 nm the densities are calculated by Beer-Lambert's law.

Plasma kinetics are modeled by incorporating a time-dependent Boltzmann equation solver into a MATLAB in-house zero dimensional chemical solver tool. A time-dependent solution of the Boltzmann equation is essential when ns-pulse excitation is used. Since such excitation is the motivation of this work, creation of such a global model was essential. After establishing the plasma kinetics solver, it was tested against the currently used gold standard in zero dimensional plasma modeling: ZDPlasKin. The downside of ZDPlasKin is the use of a Boltzmann solver that relies on local field approximation and is not time-dependent. The

newly developed solver uses LOKI-B, a time-dependent Boltzmann solver. The comparison to ZDPlasKin showed good agreement on the published examples of dynamic plasma chemistry. This validation showed that the development of the chemical kinetics solver was successful. In a first attempt to make use of the solver for $O_2(^1\Delta_g)$ chemistry, a published model was evaluated. However, at the end of this thesis, the chemistry set did not yet converge. The solver developed in this work, includes a graphical user interface (GUI) for convenience.
In the end, this thesis sets the building blocks for ns-pulse combined with RF power supply for electrical excitation of atmospheric pressure He:O_2 plasmas, $O_2(^1\Delta_g)$ detection in its effluent and global kinetics of bulk plasma species densities compatible with its electrical excitation; progressing toward greater control over produced reactive species.

TABLE OF CONTENTS

DEDICATION iii

ACKNOWLEDGEMENTS iv

RÉSUMÉ v

ABSTRACT vii

TABLE OF CONTENTS ix

LIST OF TABLES xii

LIST OF FIGURES xiii

LIST OF SYMBOLS AND ACRONYMS xvi

LIST OF APPENDICES xvii

CHAPTER 1 INTRODUCTION 1
- 1.1 Definitions and key concepts 1
  - 1.1.1 Non-equilibrium plasma 1
  - 1.1.2 Zero dimensional plasma kinetics 3
  - 1.1.3 $O_2(^1\Delta_g)$ (Singlet delta oxygen) 3
  - 1.1.4 Electrical excitation 3
- 1.2 Challenge 5
- 1.3 Research objectives 9
- 1.4 Thesis plan 9

CHAPTER 2 LITERATURE REVIEW 11
- 2.1 RONS in atmospheric pressure plasmas 11
  - 2.1.1 RONS in biomedicine 11
  - 2.1.2 RONS in agriculture 11
  - 2.1.3 RONS in plasma-assisted combustion 12
- 2.2 $O_2(^1\Delta_g)$ and ozone detection 12
- 2.3 Plasma kinetics modeling 13
  - 2.3.1 Electron Boltzmann equation solvers 13

2.3.2 Chemistry solvers 15
2.4 Pulsed power supplies 17
2.4.1 Marx generator 17
2.4.2 Blumlein generator 18
2.4.3 Magnetic pulse compression 18
2.4.4 Solid state switching 20
2.4.5 Diode opening 20

CHAPTER 3 DETAILS OF THE SOLUTION 22
3.1 High voltage pulse power supply 22
3.1.1 Input voltage and isolation 22
3.1.2 Cockcroft-Walton generator 22
3.1.3 MOSFET switch and output circuit 24
3.1.4 Test Plasma Reactor 25
3.2 Plasma kinetics 25
3.2.1 Basic structure 26
3.2.2 Graphical user interface 27
3.3 $O_2(^1\Delta_g)$ and ozone detection 27
3.3.1 Macro Atmospheric Pressure Plasma Jet 27
3.3.2 Power supply 27
3.3.3 UV absorption of Ozone 28
3.3.4 NIR emission of $O_2(^1\Delta_g)$ 29

CHAPTER 4 THEORETICAL AND EXPERIMENTAL RESULTS 31
4.1 Pulse power supply 31
4.1.1 CW generator 31
4.1.2 MOSFET switching circuit 33
4.1.3 End-to-end solution 35
4.2 O_3 and $O_2(^1\Delta_g)$ measurements with RF excitation 38
4.2.1 Ozone 43
4.2.2 $O_2(^1\Delta_g)$ 46
4.3 Plasma kinetics modeling 48

CHAPTER 5 CONCLUSION 54
5.1 Summary 54
5.2 Limitations 55
5.3 Future Research 56

REFERENCES 58

APPENDICES 63

LIST OF TABLES

Table 4.1 Zdplaskin's 1st example reactions. 50
Table 4.2 ZDPlasKin's second example reaction set. 53
Table A.1 Components for the CW generator. 64
Table A.2 Components in the BEHLKE switch control circuit. 65
Table Table B.1Reactions and corresponding rates for a He/O_2 plasma model [1]. . . 66

LIST OF FIGURES

Figure 1.1 Different plasma regimes as function of electron temperature and particle density [2]. 2
Figure 1.2 Electronic configuration comparison of the first excited state and the ground state of molecular oxygen. 4
Figure 1.3 Different discharge regimes as a function of voltage [V] and current [A] [3]. 5
Figure 1.4 Schematic of catalase inactivation by plasma generated $O_2(^1\Delta_g)$. . . . 6
Figure 1.5 Electron energy loss fraction in an RF field at atmospheric pressure and room temperature for a He plasma with 1% O_2 admixture calculated with Bolsig+ [4]. 8
Figure 1.6 Schematic of different electrical excitations and their corresponding average electron temperature. 8
Figure 2.1 Voltage and current waveforms of a Marx generator [5]. 19
Figure 2.2 Voltage waveform from a Blumlein generator used for a pseudo-spark switch [6]. 19
Figure 2.3 Working principle of a magnetic pulse compression scheme [7]. 19
Figure 2.5 Working principle of a diode opening power supply [8]. 20
Figure 2.4 Voltage waveforms for different pulse width of a solide-state switch based power supply [9]. 21
Figure 3.1 Four Stage CW generator schematic. 23
Figure 3.2 Testing circuit of the HTS-361-01 Switch. 24
Figure 3.3 Block diagram for the control PCB of the Switch. 26
Figure 3.4 DBD reactor 3D model. 26
Figure 3.5 General structure for the chemical solver. 28
Figure 3.6 Ozone absorption setup in the effluent of an APPJ. 30
Figure 3.7 $O_2(^1\Delta_g)$ emission setup in the effluent of an APPJ. 30
Figure 4.1 Multiplication card of the CW generator. 32
Figure 4.2 Output voltage at stage 10 as a function of the input peak voltage for an open circuit load. 32
Figure 4.3 Output voltage at each stage with maximum input peak voltage for an open circuit load. 33
Figure 4.4 Two multiplication cards of the CW generator. 33

Figure 4.5 Output voltage at each stage with maximum input peak voltage for an open load with 2 cards. 34
Figure 4.6 3D model of the physical layout for the pulsing circuit. 34
Figure 4.7 3D model of a high voltage resistor with low inductance. 35
Figure 4.8 Physical layout of the pulser with the DBD reactor. 35
Figure 4.9 3D model of the control PCB for the Behlke switch. 36
Figure 4.10 Output of the CW generator with different loads as a function of stages. 37
Figure 4.11 CW output voltage for a 72.3 kΩ load for three input amplitudes. . . 37
Figure 4.12 Different amplitudes with a 72.3 kΩ load. 38
Figure 4.13 Different duty cycles with a 72.3 kΩ load. 38
Figure 4.14 Different frequencies with a 72.3 kΩ load. 39
Figure 4.15 Voltage rise and complete pulse waveform for a 72.3 kΩ load. 39
Figure 4.16 Air discharge in the DBD reactor from a pulse excitation. 40
Figure 4.17 APPJ and collector adapter with a He gas mixture. 40
Figure 4.18 Mixing chamber for helium and molecular oxygen. 41
Figure 4.19 Discharge of the APPJ in pure Helium. 41
Figure 4.20 Discharge of the APPJ in He:O_2 0.99:0.01 admixture. 41
Figure 4.21 Bulk emission setup for the APPJ. 42
Figure 4.22 Emission spectra from the bulk plasma of the APPJ in He:O_2 0.99:0.01 admixture. 42
Figure 4.23 Evolution of the principal emission lines from the bulk plasma of the APPJ with different O_2 admixture. 43
Figure 4.24 Optical setup for ozone absorption. 44
Figure 4.25 Evolution of the detected O_3 density over time for fixed conditions. . 45
Figure 4.26 Ozone density for different flow conditions and He/O2 admixtures. . . 45
Figure 4.27 $O_2(^1\Delta_g)$ detection setup: APPJ and glassware. 46
Figure 4.28 $O_2(^1\Delta_g)$ detection setup: detector and signal pre-amplifier. 47
Figure 4.29 Evolution of the detected voltage over time for fixed conditions. . . . 47
Figure 4.30 Comparison of the detected voltages for different powers and detection distance. 48
Figure 4.31 Comparison of $O_2(^1\Delta_g)$ density for different total flows, powers and measurement distances. 49
Figure 4.32 GUI main window. 49
Figure 4.33 GUI for the creation of the reaction set file. 50
Figure 4.34 GUI for the creation of the condition file. 50

Figure 4.35 Electron density comparison for the first example between ZDPlasKin and the in-house tool. 51
Figure 4.36 Species density and reduced field comparison for the second example between ZDplaskin and the in-house tool. 52
Figure 4.37 Species density evolution over time for an RF excited He:O2 0.99:0.01 mixture. 53
Figure A.1 BEHLKE switch control circuit schematic. 63
Figure A.2 BEHLKE switch control circuit PCB layout. 64

LIST OF SYMBOLS AND ACRONYMS

APPJ	Atmospheric pressure plasma jet
CAP-jet	Cold atmospheric pressure plasma jet
CW	Cockcroft-Walton
EEDF	Electron energy distribution function
FWHM	Full width half maximum
GUI	GUI
IGBT	insulated-gate bipolar transistor
MOSFET	Metal-Oxydide Semiconductor field-effect transistor
NIR	Near infrared
ns	Nano-second
NT	Non-Thermal
PCB	Printed circuit board
RF	Radio frequency
RMS	Root mean square
RONS	Reactive oxygen and nitrogen species
Td	Townsend
TTL	Transistor-transistor logic
UV	Ultra-Violet

LIST OF APPENDICES

Appendix A Electrical schematics and components 63
Appendix B Plasma kinetics 66

CHAPTER 1 INTRODUCTION

NT plasmas have been studied extensively in the last 50 years for their truly unique way to electrify chemistry and their numerous potential applications covering a wide array of fields like combustion, agriculture, medicine, and materials science [10] [11] [12]. Despite these collective efforts, the fundamental mechanisms of NT plasmas remain poorly understood. This thesis aims to better understand this multidisciplinary field by achieving control over the generated species of NT plasmas with a particular focus on the effect of the electrical excitation, the sensitive detection of key species, and the modeling of their reaction kinetics in cold atmospheric pressure plasma jet (CAP-Jet)s. In this chapter, the thesis' key concepts and definitions are addressed along with the core challenge that motivated this work. The research objectives are defined, as well as the thesis plan.

1.1 Definitions and key concepts

1.1.1 Non-equilibrium plasma

Plasma, often referred to as the fourth state of matter, is an ionized gas. In 1928, Irving Langmuir used for the first time the term plasma to describe an ionized gas. Ionized means that at least one electron is striped from the molecule, resulting in a positive ion [13]. Today, the definition of plasma is given by a set of charged species that exhibit collective behavior and is globally quasi-neutral. The ionization degree of atmospheric pressure plasmas ranges from 10^{-7} to 10^{-4}, resulting in typical electron densities of 10^{11} to 10^{15} /cm^3.

Plasmas possess different properties on the basis of the conditions in which they are created. The pressure, temperature, and electric field are key parameters that determine the plasma regime. Whether in nature or in the laboratory, there are numerous examples that illustrate these different regimes. Aurora borealis, lightning, and the sun are the most commonly mentioned naturally occurring plasmas. In a laboratory, multiple regimes can also be created, some more easily than others. These different regimes are shown in the figure 1.1. Since the envisioned application of this work can be linked to bio-medicine, the plasma regime of interest is at atmospheric pressure and close to room temperature. Plasmas operating at atmospheric pressure also find increasing use in agriculture, for which the proposed control over the plasma reactivity is relevant. For such applications, scale-up is a necessity.

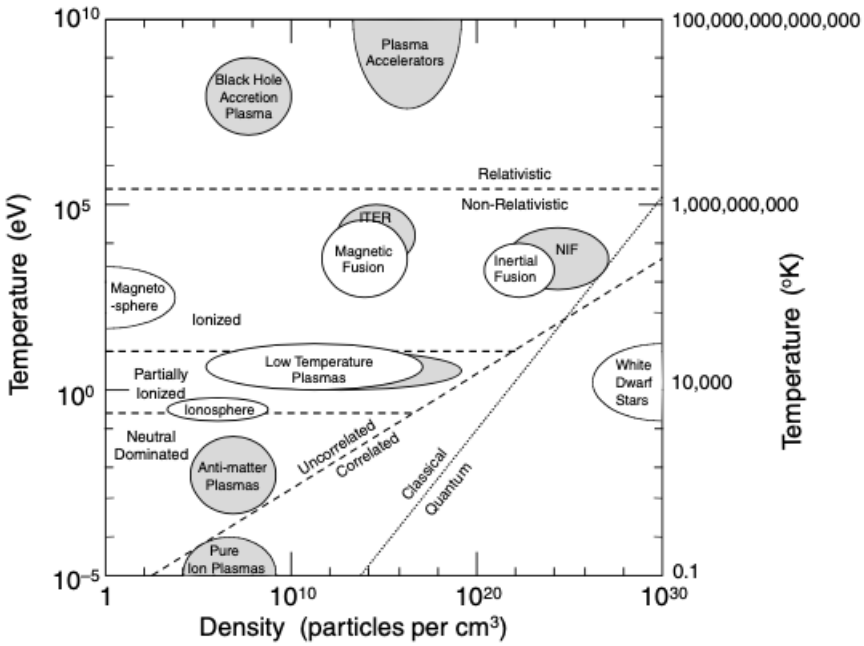

Figure 1.1 Different plasma regimes as function of electron temperature and particle density [2].

NT plasmas are described by multiple synonym terms such as non-equilibrium plasmas, cold plasmas, weakly ionized gas. They all describe a plasma in which the constituting components are not in thermodynamic equilibrium. Electrons are accelerated by the electric field and reach an electron temperature of thousands of Kelvins while the heavier particles; ions, neutrals and negatively charged species are essentially stationary in the electric field compared to the electrons, resulting in a bulk plasma close to room temperature. A more convenient way to express electron temperature is in eV, which converts to Kelvins by a factor of 11 600 K for 1 eV at a Boltzmann distributed energy. Typical electron temperatures of NT plasmas at atmospheric pressure are around 2-5 eV [13].

In a NT plasma, the electronic temperature is derived from the velocity distribution function. The probability of an electron having a certain speed is regulated by a Maxwell-Boltzmann distribution. Therefore, to describe the electron energy in a plasma, an electron energy distribution function (EEDF) that follows the Maxwell-Boltzmann distribution is needed.

1.1.2 Zero dimensional plasma kinetics

In plasma chemistry, regular chemical reactions are responsible for a variety of production pathways of chemical species. The rate of these reactions can be calculated or measured experimentally because they depend on the reactants densities and the reaction constant, which is a function of pressure and temperature. However, because the ionization degree in atmospheric pressure plasmas can be around 10^{-4}, a significant amount of free electrons are present and subsequent processes are crucial. Induced by direct electron impact, processes such as ionization, excitation and attachment electrify the chemistry and create various radicals, metastables, and charged species. The reaction rate of these processes is highly dependent on the EEDF. The rate is calculated using the following formula:

$$X = \int_{E_{th}}^{\infty} \sigma(E) \sqrt{\frac{2E}{m_e}} f(E) dE \,, \tag{1.1}$$

where E_{th} is the threshold energy for the reaction, $\sigma(E)$ is the reaction cross-section taken from a database, E is the electron energy, m_e is the electron mass and $f(E)$ is the EEDF. With the reaction rates of thermal chemistry and electronic induced chemistry, a set of coupled rate equations can be solved. This approach to plasma kinetics considers a plasma without boundaries and without variation in its properties from one spacial point to another; hence the 0D solution. Further details on the modeling of 0D plasma kinetics is given in section 2.3.

1.1.3 $O_2(^1\Delta_g)$ (Singlet delta oxygen)

$O_2(^1\Delta_g)$ is the first excited state (figure 1.2a) of molecular oxygen. Compared to the ground triplet state (figure 1.2b), the shared electrons are attributed to the same atom of oxygen and possess opposite spins. A schematic of the electrons of these two states is shown in figure 1.2. $O_2(^1\Delta_g)$ has a lifetime close to 75 minutes. It is relatively long because the transition to the ground triplet state is quantumly forbidden by the selection rules. The relevance of this excited state in NT plasmas applications is described later in section 2.1.

1.1.4 Electrical excitation

All plasmas are created through the free electrons present in the gas from radiation ionization. These few free electrons are accelerated by the potential applied between two electrodes, and when this potential is sufficient, they themselves create secondary free electrons by colliding with neutral or excited states. More free electrons are created at the cathode and this results

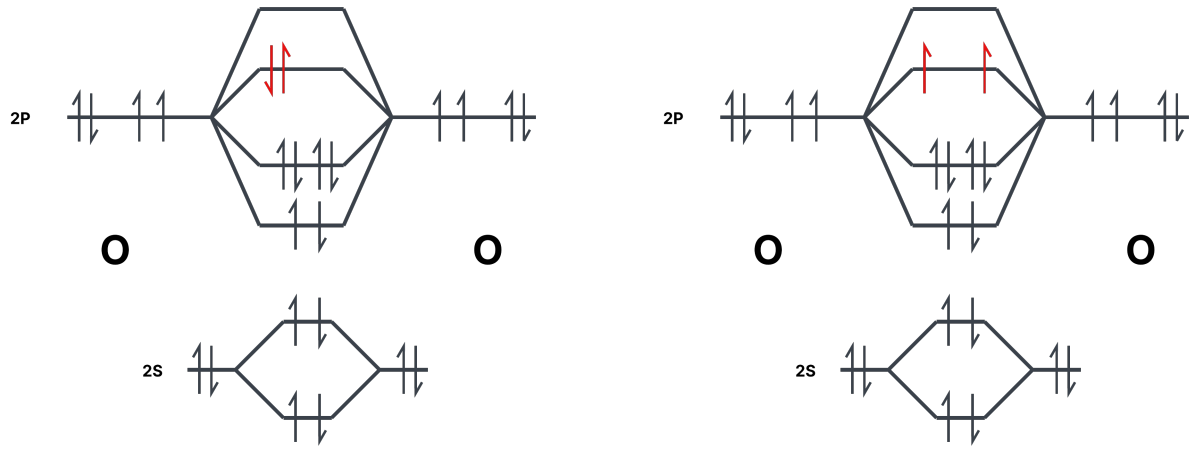

(a) First singlet state: $O_2(^1\Delta_g)$

(b) Triplet state: Molecular oxygen

Figure 1.2 Electronic configuration comparison of the first excited state and the ground state of molecular oxygen.

in an electron avalanche until a self-sufficient discharge is achieved.
Depending on the potential, the current passing through the discharge and the electrode geometry, different types of discharge are observed. Different discharge regimes are shown in figure 1.3. In a two electrodes geometry, the dark discharge is typically a streamer. When the potential is increased, it reaches a sustained discharge and the gas becomes conductive, which quickly decreases the voltage. Then, as the current increases, the voltage stays constant because the area occupied by the plasma between the electrodes is growing. This regime is called the glow discharge and is a typical plasma mode of NT plasmas. When the electrode area is fully occupied by plasma, then an increase in the current again results in a voltage rise. If the current and voltage are too high, the discharge transitions to an arc (thermal plasma).

To keep the plasma from transitioning into an arc, one has to limit the current. A corona discharge for example, is achieved by rapidly reducing the electric field between the electrodes. This is due to the electrode geometry with one sharp electrode of small dimensions and the second electrode with rounded and larger dimensions. Another way is to add a dielectric at one or both the electrodes, which prohibits a current flow. A radio-frequency (RF) excitation serves the same purpose: with a frequency in the MHz region, the field oscillates fast enough to prevent current build-up and sustain a glow, NT discharge.

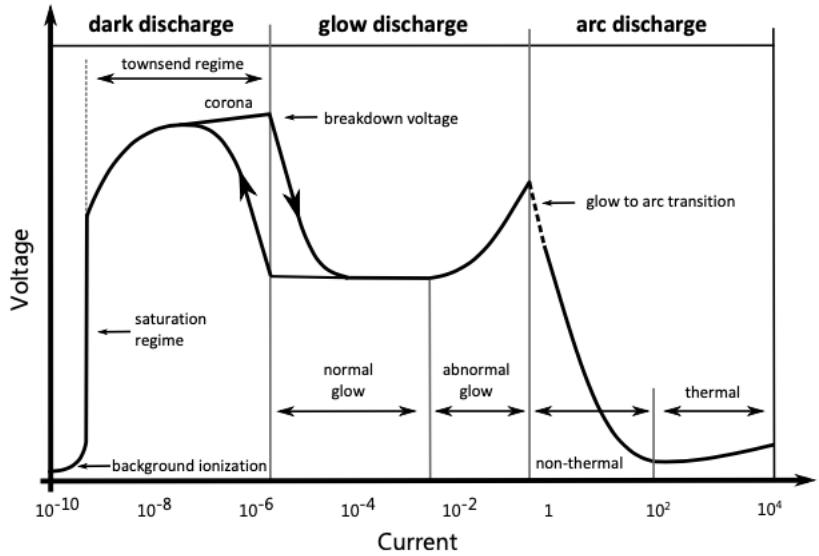

Figure 1.3 Different discharge regimes as a function of voltage [V] and current [A] [3].

1.2 Challenge

The reactive oxygen and nitrogen species produced by NT plasma at atmospheric pressure are of great relevance to the biomedical and agricultural field. In the following paragraphs, two examples are chosen from the literature to highlight the importance of reactive oxygen and nitrogen species (RONS) and the benefit of controlling their generation, with special focus set on $O_2(^1\Delta_g)$.

Bauer et al. were one of the first to identify key RONS and the biochemical pathways that lead to cancer cells apoptosis following a NT plasma treatment in [14]. They report in that article that NT plasma present a great selectivity, as seen in figure 9 of [14]. The $O_2(^1\Delta_g)$ created by the plasma source locally inactivates membrane-associated catalase, an enzyme present in cancerous cells. These cells, deprived of their main protection against oxidative stress, allow H_2O_2 and $ONOO^-$, generated by the plasma, or by the cells, to respectively react and create secondary $O_2(^1\Delta_g)$. With this cyclic inactivation mechanism, oxygen peroxide (H_2O_2) can enter the cells and induce signaling pathways leading to apoptosis. This process is schematized in figure 1.4.

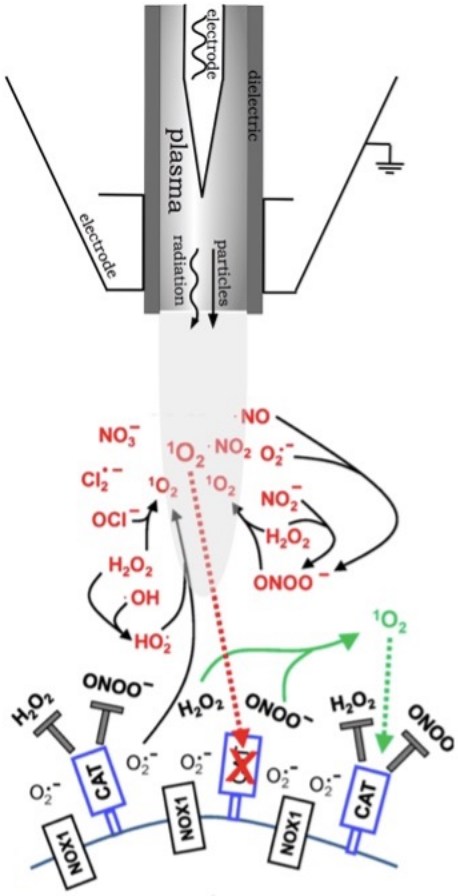

Figure 1.4 Schematic of catalase inactivation by plasma generated $O_2(^1\Delta_g)$.

A key point is that healthy cells that receive the same plasma treatment do not go into apoptosis. The biochemistry involved in this multi-step process is very complex and go beyond the scope of this work, yet the main takeaway is that control over the generation of $O_2(^1\Delta_g)$ is crucial and could lead to more efficient cancer therapy or even patient-tailored therapy.

Gao et al. review the beneficial effects of the RONS created by NT plasmas and transferred to water in the agricultural and food industry [15]. Again, the plasma-liquid interactions involved in the plasma-activated water process go beyond the scope of this work, yet it becomes clear that RONS are highly relevant and can benefit seed germination and plant growth, as well as protect against microbial exposure. Control over the generation of RONS such as OH^*, NO^*, NO_2, $ONOO^-$ as well as $O_2(^1\Delta_g)$ is crucial.
Because of its relevance in both fields, the control over the production of $O_2(^1\Delta_g)$ is the main focus of this thesis. The challenge is to advance the three fundamental components necessary

to design a plasma source that allows to precisely control its $O_2(^1\Delta_g)$ output.

To achieve such a control, we must first be able to detect this molecule. A key aspect of this work is to set up a sensitive detection scheme of $O_2(^1\Delta_g)$ based on infrared light emission [16]. $O_2(^1\Delta_g)$ transition to ground state being forbidden, only a small amount of light is emitted from $O_2(^1\Delta_g)$ generated by the plasma, and therefore the detection setup must be sensitive.

Figure 1.5 shows the electron energy loss-fraction into different chemical pathways, of a helium and oxygen plasma, simulated with Bolsig+ [17], at atmospheric pressure and room temperature with an RF excitation field. This simulation demonstrates that processes in which the electron energy is deposited vary with field amplitude. For a 1% admixture of molecular oxygen in helium, the electron energy loss-fraction simulation shows that at a reduced field of 4.5 Td (Townsend), most of the electron energy is deposited into producing $O_2(^1\Delta_g)$ (apart from gas heating, which is not shown). 4.5 Td corresponds to an electron temperature of 2 eV. This is a relatively low electric field and, depending on the electrode geometry, it is often below the breakdown voltage required to create a plasma. RF plasmas operate at higher reduced electric fields and thus cannot produce $O_2(^1\Delta_g)$ at maximal efficiency. This means that another electrical excitation is required. A solution to produce $O_2(^1\Delta_g)$ efficiently is to couple a short high voltage pulse with a low electric field RF signal. The short pulse excitation induces breakdown (although electric fields are far too large to produce $O_2(^1\Delta_g)$ efficiently), and the RF voltage sustains the plasma over a considerable amount of time at electric fields ideal for channeling electron energy into $O_2(^1\Delta_g)$ generation, which would normally be too low for plasma breakdown. In summary, the short pulse initiates the plasma and the low field RF excitation produces $O_2(^1\Delta_g)$ efficiently. This approach is defined as pulse-sustained excitation. Figure 1.5 shows pulse-sustained excitation in comparison to RF excitation mode, along with the typical corresponding electron temperatures.

The present work establishes two major cornerstones for the pulse-sustained approach: the development of a pulsed power supply, and the development of a plasma chemical model that enables the simulation of a pulse-sustained plasma excitation.

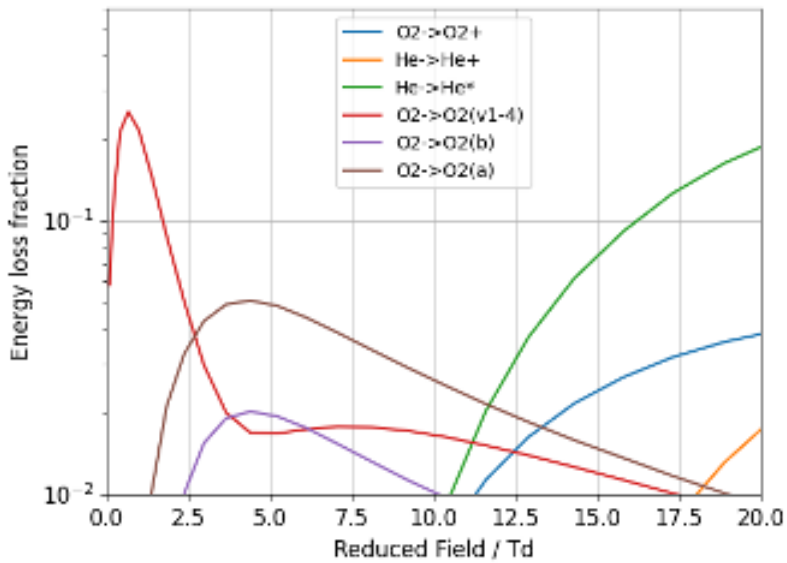

Figure 1.5 Electron energy loss fraction in an RF field at atmospheric pressure and room temperature for a He plasma with 1% O_2 admixture calculated with Bolsig+ [4].

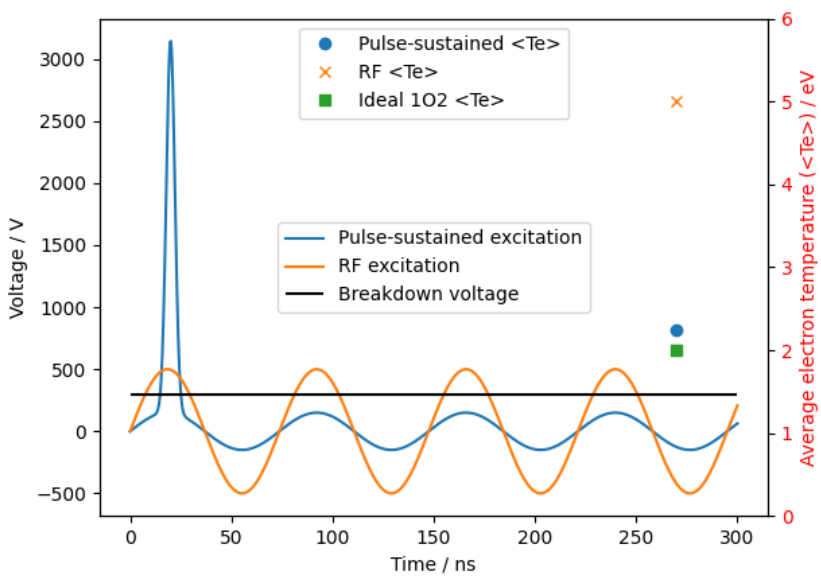

Figure 1.6 Schematic of different electrical excitations and their corresponding average electron temperature.

1.3 Research objectives

To gain control over the electric field and to apply this power supply to different plasma sources and gas composition, it has to be flexible. The amplitude, length, and repetition of the pulse need to be adjustable. In view of future applications in plasma for agriculture, the power supply also has to be scalable and parallelizable.
To understand the production and destruction mechanisms of $O_2(^1\Delta_g)$, a 0D plasma kinetics model is needed. Because of the short-pulse excitation, the local field approximation usually used in Boltzmann solvers, fails. A 0D plasma kinetics model will need an included time-dependent Boltzmann solver. To the best of our knowledge, such an open source plasma kinetics model does not yet exist.
In this work, detection of $O_2(^1\Delta_g)$ is achieved by following the approach of Sousa et al. [16]. Thorough optical alignment and filtering of electrical noise, as well as the use of an in-house signal amplifier for the NIR photodiode used for detection of the light emission, we achieved an improvement of the signal-to-noise ratio over existing works.

The objectives of this thesis are the following:

1. **Develop a flexible, modular and scalable pulsed high voltage power supply**
2. **Establish a time-dependent chemical reaction global solver for plasma kinetics**
3. **Set up a $O_2(^1\Delta_g)$ NIR emission spectroscopy in the effluent of an atmospheric pressure plasma jet**

The objectives described above constitute the foundation for designing a pulse-sustained power supply and a time-dependent plasma chemistry model that will accompany it. Full implementation does not fit in the time frame of this thesis and is kept in mind for future work.

1.4 Thesis plan

This thesis has the three following sections: In the literature review, in section 2.1, the relevance and generation of reactive oxygen and nitrogen species (RONS) in plasmas are described. Section 2.2 shows how key RONS, namely $O_2(^1\Delta_g)$ and O_3 are detected by optical methods. Section 2.3 gives an overview of reaction kinetics modeling and the final section of the literature review describes the state of the art of pulsed high voltage power supplies.

Chapter 3 describes the foundations for the approaches used in this thesis on the three core aspects of plasma reactivity control, which are the power supply, the $O_2(^1\Delta_g)$ and ozone detection and the modeling. These aspects form the cornerstone of plasma control. The solutions chosen in this work for each of the three aspects are described and evaluated over existing approaches. Chapter 4 presents the results and outcomes of the thesis. In the final chapter of the thesis, a summary and conclusion is given along with suggestions on how the findings of this work will lead to a precisely controllable plasma source.

CHAPTER 2 LITERATURE REVIEW

In this chapter, key developments around NT plasmas and there usage in biomedicine and agriculture are briefly examined. Particular focus is given to $O_2(^1\Delta_g)$ detection, global model of plasma kinetics and ns power supplies as they are the foundation of this work.

2.1 RONS in atmospheric pressure plasmas

2.1.1 RONS in biomedicine

NT plasmas at atmospheric pressure are used in biomedicine. The plasma temperature is sufficiently low to not cause thermal damage to exposed tissue. The RONS produced in the bulk plasma or in the effluent are comparable to the species active in intra-cellular signaling pathways in humans. So the ability to precisely control the RONS in the gaseous phase is expected to lead to targeted therapy for multiple illnesses [18]. The significance of plasma generated $O_2(^1\Delta_g)$ has been pointed out for plasma based cancer therapy, since it could be one of the key species responsible for the plasma's selectivity [14]. $O_2(^1\Delta_g)$ detection is key, especially in biomedicine, as it is one of the few species still present, at a certain distance, in the effluent of atmospheric pressure He/O_2 plasmas. As reported in [19], some metastables of helium can play a role in plasma sterilization, and different cell interactions. However, at a certain distance, as is often the case in biomedicine applications, most of these metastables have collided and transferred their energies to other species. This behavior, is shown in [20], where the rapid drop of helium metastables densities in a He/O_2 mixture is highlighted. Also, the authors in [21] show that atomic species have recombined at a certain distance, leaving mostly $O_2(^1\Delta_g)$ and O_3. Because the density of these two species respectively vary with distance due to quenching effects, varying the treatment distance is a great way to isolate the effect of $O_2(^1\Delta_g)$ on the end-application.

2.1.2 RONS in agriculture

Multiple applications of NT plasmas are being researched in the agricultural field, including accelerated seed germination, plant growth, decontamination, pesticide replacement or even prolongation of shelf life. A lot of geometries and electrical excitations for the plasma reactors are investigated, usually they are operated at atmospheric pressure. The RONS produced by the plasma in the gaseous phase are often transferred to liquid such as hydroponic solution, which is then used for the desired application. The RONS content of this plasma activated

water is tightly linked to the RONS initially at the gas/water interface. Nitrate, nitrite, hydrogen peroxide, ozone, $O_2(^1\Delta_g)$ and other radicals are reported key actors in [22] for chemical pathways of plants and seed cells.

2.1.3 RONS in plasma-assisted combustion

Plasma-assisted combustion has gained a lot of traction in the last two decades because of the wide array of possible applications. Applications field reaching from aerospace propulsion to fuel reforming, plasma-assisted combustion proved to be a useful way to gain control over combustion processes. In this research, multiple type of discharges and electrical excitation over a huge range of gas pressure are studied. In the same way as for the other applications, this field aims to study the dynamics of production and destruction of certain reactive species, initially created by electron impact, and use this understanding to favor specific chemical pathways. It is reported in [23] that ozone and $O_2(^1\Delta_g)$ added to the flow of a burning flame does impact flame height and flame speed. It is also reported that $O_2(^1\Delta_g)$ plays a key role in accelerating combustion processes.

2.2 $O_2(^1\Delta_g)$ and ozone detection

Only few $O_2(^1\Delta_g)$ detection methods are established, especially in the gaseous phase. A brief overview of these methods with their limits and challenges is presented below.

$O_2(^1\Delta_g)$ generation and diffusion can be monitored at single cell level in by one photon microscopy, two photon microscopy and array-based imaging microscopy. Also, a microscope is described in [24] for $O_2(^1\Delta_g)$ detection, where photon counting is used at 1270 nm to resolve densities. These techniques allow for time and space resolved signals related to $O_2(^1\Delta_g)$ density but possess a great number of components and are rather complex.

In 2004, densities of $O_2(^1\Delta_g)$ were measured by cavity-enhanced absorption. More precisely, off-axis integrated cavity output spectroscopy was used to measure densities from 4^{13} molecules/cm^3 produced by an 13.56 MHz RF excited inductively coupled plasma with 5% Oxygen admixture. The power used was 250 W and the flow 3 SLM. The cavity was 82 cm long and bounded by two highly reflective mirrors. A single mode 1505 nm diode laser was used. The light leaving the cavity is then collected by an InGaAs photodiode. With complex calculations the authors were able to link this collected profile to an absolute density [25].

Development of chemical probes for $O_2(^1\Delta_g)$ detection has been accelerated in recent years due the specie relevance in biochemical processes. Numerous commercially available probes,

notably Singlet Oxygen Sensor Green (SOSG), can be used to determine $O_2(^1\Delta_g)$ densities in the aqueous phase. However, these reportedly lack specificity [26].

$O_2(^1\Delta_g)$ can be detected in the gaseous phase by NIR emission spectroscopy. By observing the transition to the ground state at 1270 nm with a narrow band pass filter, from a detection cell with an InGaAs photodiode, a voltage is measured. The voltage is correlated to an absolute density in the cell via a ray-tracing Monte-Carlo algorithm that attritubes a probability of an emitted photon to reach the detector [27]. The detection limit of this method is estimated at $2 * 10^{13}$ per cubic centimeter [16].
Due to rapid collisional quenching of $O_2(^1\Delta_g)$ by ozone, particular interest in ozone density is required, especially when detection setup is in the effluent of an atmospheric pressure plasma device. Absolute densities of ozone are easily detected by absorption spectroscopy in the UV at 254 nm. Aside from collisional quenching of the excited $O_2(^1\Delta_g)$ state, ozone molecules absorb the light emitted at 1270 nm by the ground transition of singlet oxygen as defined in [28].

2.3 Plasma kinetics modeling

Plasma kinetics modeling is widely used to validate experimental results or to gain insight into the complex processes taking place inside a NT plasma. Models in which the spatial derivatives of the fluid equation are neglected are called global models. These volume averaged models are easier to implement and significantly less computationnally expensive than space-resolved ones [29]. From these zero-dimensional models, fundamental electron swarm parameters, such as electron drift velocity, electron mobility, and electron diffusion coefficient can be investigated. With these swarm parameters driving the rate coefficients of electron impact-induced processes, species densities can be obtained and a chemical model can be produced.

2.3.1 Electron Boltzmann equation solvers

Multiple Boltzmann solvers exist in literature. Their objective is the same; to solve the electron Boltzmann equation to obtain the non-Maxwellian EEDF and compute the electron swarm parameters. The Boltzmann equation is:

$$\frac{\partial f}{\partial t} + \vec{v} \cdot \nabla f - \frac{e}{m_e} \vec{E} \cdot \nabla_v f = C[f], \tag{2.1}$$

where f is the electron distribution, v is the velocity vector, e and m_e are the electron charge and mass, E is the electric field, ∇_v is the velocity gradient and C is the change in f due to collisions. To solve equation 2.1, all solvers make simplifications and approximations. Some Boltzmann solvers and their limitations are discussed below.

Bolsig+

Bolsig+, a Fortran 90 based program, was developed in 2005 by Hagelaar et al. and proved to be a powerful and efficient tool to compute EEDFs and electron swarm parameters [17]. To solve equation 2.1, Bolsig+ assumes a uniform field across the mean free path and equal collision probabilities in space. The Boltzmann equation can then be written as

$$\frac{\partial f}{\partial t} + v\cos\theta\frac{\partial f}{\partial z} - \frac{e}{m_e}E(\cos\theta\frac{\partial f}{\partial v} + \frac{\sin^2\theta}{v}\frac{\partial f}{\partial\cos\theta}) = C[f]\,, \tag{2.2}$$

where v and E are now magnitudes, θ is the angle between the velocity and the electric field while z is the position in the field direction.
To simplify the time dependency of equation 2.2, a uniform field is assumed (constant or oscillating electric field). Also, to simplify the θ dependency, f is expanded with Legendre polynomials around $\cos\theta$. Only the first two terms of this expansion are kept by Bolsig+. This is called the two-terms Boltzmann approximation and is used by multiple Boltzmann solvers. Validity of this simplification is discussed later. More details on how the swarm parameters are calculated by Bolsig+ can be found in [4].

Bolos

Bolos, written by Alenjandro Luque is a Boltzmann solver based on Bolsig+, also available as freeware. It uses the same algorithms and simplifications but is coded in Python instead of being a binary executable. However, it is slower than Bolsig+. Bolos has recently been written in C++ by Xiao Shao. The resulting tool is called CppBolos with an even greater speed than the original Bolsig+. Bolos and CppBolos are essentially Bolsig+ but in different programming languages.

Multibolt

Multibolt [30] is also a Boltzmann equation solver. Most of the simplifications are the same, the applied electric field is constant and from that results steady-state condition. However, multiple terms are kept when dealing with the Legendre expansion. Usually, ten terms are

kept, resulting in more accurate results while being a bit more computationally expensive.

Loki-B

Loki-B was developed as an open source Boltzmann equation solver written in MATLAB [31]. As Bolsig+ and MultiBolt, Loki-B makes approximations to compute the EEDFs and the swarm parameters like the steady-state condition. It uses the two terms Boltzmann approximation like Bolsig+. However, in the lastest version, the authors included a feature to solve the time-dependent Boltzmann equation, allowing users to use non-uniform electric fields.

Monte Carlo and validity of approximations

Solving equation 2.1 is not the only way to obtain EEDFs and swarm parameters. In recent years, Monte Carlo simulations were used to obtain electron transport in different gas mixtures for a given electric field. METHES [32] and Loki-MC [33] are great examples. Monte Carlo tools are taken as the golden standard when compared to electron Boltzmann equation solvers because they are exact solutions, aside from numerical noise and statistical errors. To analyze the validity of the main assumptions made by Boltzmann solvers, they are compared to LOKI-MC in [34]. When simulating short electric pulses (like ns-pulses), these approximations do not hold for the full length of the pulse. The local field approximation and the local mean energy approximation fail with very fast changing electric fields, leading to poorly estimated EEDFs and can lead to inaccurate rate coefficients and densities by tens of percent if included in a chemical model. The time-dependent solver of Loki-B was also compared and gave the closest results to the exact solution. The only region where Loki-B fails to capture the transport dynamics is at the beginning of the pulse (0 to 0.2 ns). It is important to note that Monte-Carlo solvers are not usually included in chemical models because of their massive computational cost.

2.3.2 Chemistry solvers

From a set of chemical reactions and for given conditions, chemical solvers determine the evolution of densities through time. They consider thermal chemistry where the rate coefficients are known from literature but also electron impact-induced reactions whose rate coefficients are calculated by an integrated Boltzmann equation solver.

ZDPlasKin

Zero-Dimensional PLASma KINetics is a powerful tool to investigate NT plasma kinetics [35]. Intended as a semi-black-box code written in Fortran 90, it has been widely used since its release in 2008. ZDPlasKin incorporates Bolsig+ as the Boltzmann solver. It requires the user to input a text file containing the reactions to consider, the electron impact reaction cross-section to be considered by Bolsig+ as well as a condition file in Fortran 90. For j reactions and i species, the variation of a species density N is determined by the following equations.

$$aA + bB \rightarrow a'A + cC \tag{2.3}$$

Where A,B and C are arbitrary species.

$$R_{ij} = k_j[A]^a[B]^b \tag{2.4}$$

Where k_j is the j reaction constant, [X] is the species X density and R_{ij} is the reaction coefficient.

$$Q_A = (a' - a)R \tag{2.5}$$

$$Q_B = -bR \tag{2.6}$$

$$Q_C = cR \tag{2.7}$$

Where Q_i is the source term of species i in reaction j.

$$\frac{d[N_i]}{dt} = \sum_{j=1}^{j_{max}} Q_{ij}(t) \tag{2.8}$$

ZDPlasKin is a flexible and fast tool for simulation species densities evolution. In recent versions, a visualization tool has been included to facilitate data processing. However, the multi-step compilation is tedious, and the black-box preprocessor is not supported on new operation systems anymore. Fortran 90 is not a trivial language, and most of the flexibility of ZdPlaskin comes from writing conditions and master files in Fortran 90.

ChemPlasKin

ChemPlasKin [36] is a tool created to simulate gaseous densities over time with a particular focus on ns-pulse electric field excitation. Intended as a simulation tool for plasma-assisted combustion, the infrastructure for a user-defined number of pulses is included. ChemPlasKin

combines at the source code level two other tools CppBolos and Cantera. CppBolos was described earlier, it is Bolsig+, written in Python then written in C++. Cantera is a well-known transport chemistry solver in the combustion community. Very fast results of densities after a pulse train are observed (3 times faster than ZDPlasKin), CppBolos still uses the steady-state approximation. Also, ChemPlasKin is written in C and C++ and the user has to input and modify conditions files which is not trivial for the average user.

2.4 Pulsed power supplies

Nanosecond (ns) pulse discharges have been widely studied in the past two decades for their unique way to electrify chemistry. The design of such power supplies is still being investigated. Although commercial power supplies are available for purchase, namely from FID GmbH and Eagle Harbor Technologies, the high cost and rigidity of these solutions make them unsuitable for applications requiring scale-up or versatility. For that reason, multiple plasma research groups develop their own in-house ns-pulse power supply to achieve tailored pulse characteristics. A ns-pulse is characterized by its pulse shape, amplitude, width, repetition frequency, as well as rise and fall times. Presented in this section are the different strategies used by the plasma community to achieve high voltage ns-pulse excitations.

Numerous detailed review articles exist on pulsed power supplies used by the plasma community to create discharges. This section is based on two; [37] briefly discusses the working principles, while [7] goes into more details and shows typical voltage waveforms. They agree on 5 topologies; Marx generators, Blumlein configuration, magnetic pulse compression, solid-state switching, and diode opening. Some examples of these topologies are presented below, highlighting their advantages and disadvantages.

2.4.1 Marx generator

Developed by Erwin Otto Marx in 1924, the Marx generator is still used today in the plasma community to create ns-pulse excitation. A Marx generator charges multiple capacitors in parallel via a DC voltage source and discharges them in series to create a high voltage pulse. The change between parallel and series configurations is carried out by a switch assigned to each capacitor. The switches and their driver circuit are the critical parts. There are quite a few switching options available today, such as spark gaps and solid-state switches based on metal-oxydide semiconductor field-effect transistors (MOSFET) and insulated-gate bipolar

transistors (IGBT) technology, all resulting in square, high-voltage ns-pulses. An example where MOSFETs switches are used is in a Marx generator to produce sub-ns rise time and 10 ns pulse width with an amplitude reaching 20 kV at a pulse repetition rate of 10 Hz to produce ozone with a DBD [5]. Voltage and current waveforms taken from [5] of such a power supply are shown in figure 2.1. Although flexible, the timing control of the switches proves to be complex and requires a large total number of components.

2.4.2 Blumlein generator

Alan Blumlein demonstrated in 1937 a pulse forming network based on two transmission lines. A load is placed between two transmission lines that are charged by a high voltage DC power supply. One end of a transmission line is switched to the ground, usually by a spark gap, creating a propagating wave towards the load. The two lines ensure that the amplitude of the pulse is the same as the charging voltage. Pulse characteristics (rise time, pulse width) are dependent on the line's composition (material, length, impedance). A Blumlein generator is used in [6] to create a ns-discharges across a purely resistive load. They reached 26 kV in amplitude with pulse width of 90 ns and rise time of 25 ns at 100 Hz repetition frequency. The voltage waveform of this power supply is taken from [6] and shown in figure 2.2. Implementing such a generator is difficult. In addition, the pulse width is fixed and the pulse generator is extremely specific to the load.

2.4.3 Magnetic pulse compression

Magnetic pulse compression is usually combined together with another approach. Using a large-width pulse that passes through a saturable inductor that acts as a switch. When enough current passes through the inductor, the core saturates and the voltage drops resulting in a compression of the pulse. Used in a single stage or in a series of stages, to further compress the pulse, this principle proves to be effective in creating ns-discharges. Used in [38] for CO_2 conversion in a ns-pulse combined with RF approach, such a pulser reached 10 kV in amplitude with 75 ns rise time at 500 Hz repetition rate. Figure 2.3 demonstrates the working principle of magnetic pulse compression. However, enormous care must be taken when choosing the right component values and materials, especially the inductors. Once implemented, the pulse characteristics are not easily changed.

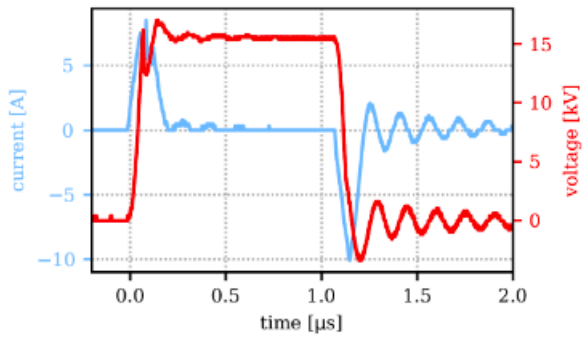

Figure 2.1 Voltage and current waveforms of a Marx generator [5].

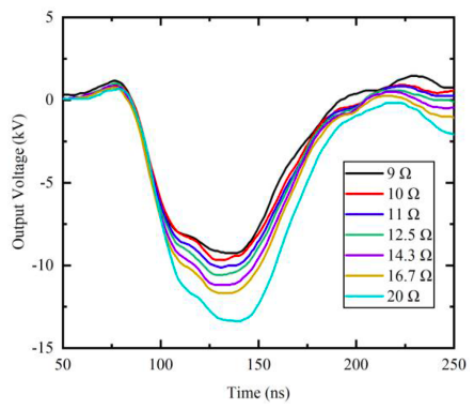

Figure 2.2 Voltage waveform from a Blumlein generator used for a pseudo-spark switch [6].

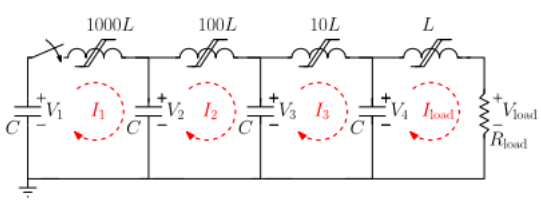

(a) Schematic of a 4 stage magnetic pulse compression

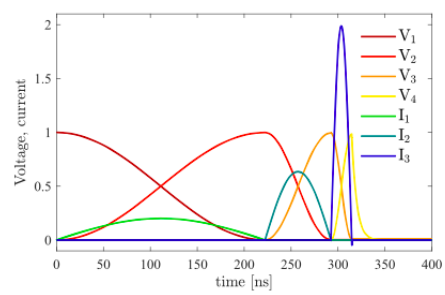

(b) Magnetic pulse compression normalized voltage and current waveforms of at four different stages

Figure 2.3 Working principle of a magnetic pulse compression scheme [7].

2.4.4 Solid state switching

Using a DC high voltage power supply, plus an array of capacitors or inductors to store energy, and discharging it via a switch, is a simple way to create pulses. Solid-state switching is based on semiconductor technology. Spark gaps or magnetic switches are also viable options. With recent advances in MOSFETs technology, switches have become more compact, efficient and fast. Available commercially at reasonable cost, these switches offer an easy way to create ns-pulse. The challenge usually lies in the control circuitry. In [9], the authors used a MOSFET-based switch from BEHLKE to turn on and off a high voltage DC (also built in-house) to create ns-pulses and ignite a DBD plasma reactor. The pulse characteristics are square pulses with 10 kV amplitude, pulse width of 350 ns and rise time of 20 ns at a repetition frequency of 4 kHz. The voltage waveforms for different pulse widths of this power supply are shown in figure 2.4.

2.4.5 Diode opening

This method uses the energy stored in an inductance and the recovery process of fast recovery drift-step diodes to interrupt the flowing current through the inductance, creating a voltage spike across it. This process utilizes the resonant charging of two LC circuits. It can create very short pulses with amplitude up to the MV. However, these diodes are expensive and the pulse characteristics fully depend on the diodes performance [7]. Figure 2.3, taken from [8] demonstrates the working principle of diode opening based power supply.

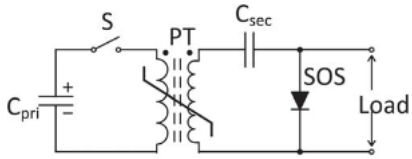

(a) Schematic of a diode opening power supply

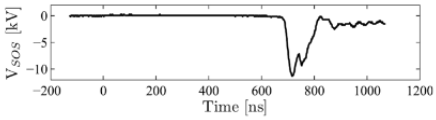

(b) Diode opening pulsed voltage waveform

Figure 2.5 Working principle of a diode opening power supply [8].

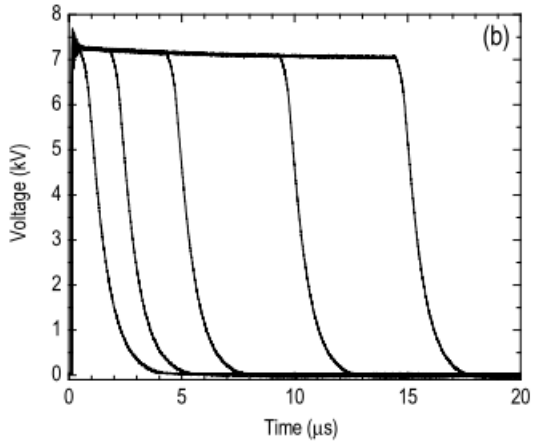

Figure 2.4 Voltage waveforms for different pulse width of a solide-state switch based power supply [9].

CHAPTER 3 DETAILS OF THE SOLUTION

In this chapter, we describe the foundations for the approaches used in this thesis on the three core aspects of plasma reactivity control, namely the power supply, the $O_2(^1\Delta_g)$ and ozone detection and, the modeling.

3.1 High voltage pulse power supply

The chosen concept for the high voltage pulse power supply is based on the design in [9]. This pulse forming network is selected because it is fully engineered and very flexible. It can adapt to multiple loads and possesses a variable amplitude, pulse width, repetition frequency, a short rise time and a relatively square pulse. The power supply is broken down into three parts: an input sinusoidal voltage, the creation of a high voltage DC, and a switching circuit to produce the pulse.

3.1.1 Input voltage and isolation

The input sinusoidal wave is chosen to be the wall outlet at 120 V RMS at 60 Hz. The signal is passed through an isolation transformer and then connected to an adjustable AC transformer called a VARIAC. The VARIAC takes an input sinusoidal wave and modulates its amplitude by 0 to 110% of the input. It is widely used for safety purposes and to test circuits at low voltage. At the output of this part is a sinusoidal wave with an adjustable amplitude from 0 to 130 V_{RMS}.

3.1.2 Cockcroft-Walton generator

The Cockcroft-Walton (CW) generator is a circuit invented in 1934 to amplify and rectify voltages. It is still used today, namely for applications requiring very high voltages and low currents like particle accelerators. The behavior of the circuit is well known and well documented. This circuit is composed exclusively of diodes and capacitors arranged in a multistage configuration. It takes, as an input, a sinusoidal wave and outputs an amplified DC voltage. The gain in voltage depends on the component values, the number of stages and the input voltage amplitude. A schematic of a 4 stage CW generator is shown in figure 3.1 as an example. When no load is connected at the output of a CW generator, the theoretical

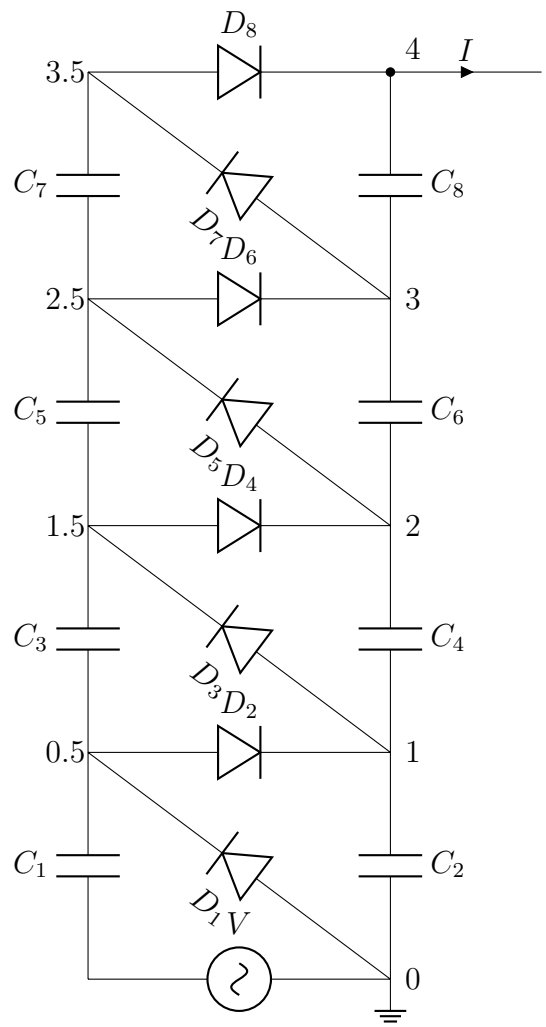

Figure 3.1 Four Stage CW generator schematic.

DC output voltage is calculated as follows:

$$V_{out} = 2nV_{peak}\,, \tag{3.1}$$

where n is the number of stages and V_{peak} is the peak value of the input sine wave. A printed circuit board for a 10 stage CW generator was designed and assembled by Yianni Hudon-Castillo, a former intern student. With the wall voltage as input and 10 stages, this circuit can act as a high voltage DC source with an output amplitude around 4 kV (calculated with equation 3.1). To reach higher amplitudes, multiple printed circuit board (PCB) can be stacked. However, when a load is connected to the CW generator, the flow of current decreases the overall output voltage, while at the same time introducing a ripple. The ripple

δV_{out} can be calculated as follows (if all capacitors have the same value):

$$\delta V_{out} = \frac{I}{fC}\frac{n(n+1)}{4}, \tag{3.2}$$

where I is the mean load current, f is the AC input frequency into the CW and C is the value of a capacitor. The global voltage drop ΔV_{DC} is calculated as follows:

$$\Delta V_{DC} = \frac{I}{fC}(\frac{2n^3}{3} + \frac{n^2}{2} - \frac{n}{6}) \,. \tag{3.3}$$

Equations 3.2 and 3.3 are important to understand the behavior of the CW generator presented in chapter 4.

3.1.3 MOSFET switch and output circuit

Once a high voltage source is created, a MOSFET switch is used to turn it on and off. In this work, a HTS-361-01 switch from BEHLKE GmbH is used. This switch can be used for a DC voltage up to 36 kV and an input current up to 12 A. It is powered with an external 5 V DC and triggered with a 5 V transistor-transistor logic (TTL) based circuit. The *on*-time and pulse frequency are set from the TTL circuit. For positive pulses, BEHLKE proposes the testing circuit shown in figure 3.2, where R1 and C1 are filtering components, C_B is a 10 nF capacitor and R_L is a load resistor with a recommended value of 5 kΩ. All resistors used in the output circuit must be inductance-free, as the switch creates a lot of electromagnetic interference. To supply the 5 V DC to the switch as well as the TTL, an in-house PCB was designed. Variable pulse frequency and duty cycle in this 5 V TTL circuit is essential, as it acts as the control for the high voltage pulse. The switch requirements for the 5 V DC

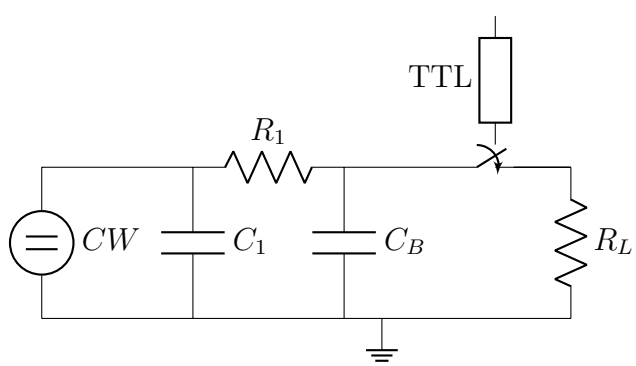

Figure 3.2 Testing circuit of the HTS-361-01 Switch.

supply are simple; it must be a voltage between 4.75 and 5.25 V DC, otherwise the switch shuts off. For the TTL, the switch accepts amplitudes between 3 and 10 V, 5 V is chosen for convenience. Fast rise and fall times of the TTL are important as the switch opens or closes when it detects a change within 15%. The proposed board is supplied by a 9 V AC/DC wall adapter. The 9 V DC is then regulated and stepped-down to 5 V DC. Part of this signal is used to power the switch while the other is used for the TTL trigger. Two NE555 timers are used. A potentiometer is associated to each one where the user can control the frequency and duty cycle by changing their values. To ensure fast rise time, the pulse is passed twice (to conserve positive polarity) in an SN74AC14N Schmitt inverter. A bypass for the 5 V DC as well as for the TTL is included. Also, a BNC connector is added to monitor the triggering signal. A block schematic is presented in figure 3.3.

3.1.4 Test Plasma Reactor

In order to test and characterize the power supply, a plasma reactor was built based on a dielectric barrier discharge. Air discharges were chosen to simplify the design and assembly of the reactor. The reactor consists of one powered electrode and one grounded electrode. In between, a dielectric was inserted. The reactor must offer a varying distance between electrodes. Two round aluminum electrodes of 30 mm in diameter were chosen arbitrarily for dimensions. The dielectric was a glass disk of 50 mm in diameter. The support for the electrodes was designed and 3D printed in PLA. The chosen electrodes were threaded for M8 screws. M8 bolts were used to make electrical connections. This design is shown in figure 3.4.

3.2 Plasma kinetics

The time-dependent solver Loki-B [31] is the best trade-off between accuracy and computational cost. Even when ns-pulse electric fields are used, this Boltzmann solver (when solving time-dependent Boltzmann equation) outputs EEDFs and swarm parameters in good agreement with the gold standard Monte-Carlo. A major drawback is that this tool does not support chemistry. To simulate plasma kinetics, the goal is to code, in MATLAB, a chemistry solver which makes use of Loki-B. It is necessary because, to our knowledge, an open source plasma chemistry tool, able to solve a time-dependent Boltzmann equation, essential with ns-pulse, does not exist. To ensure proper functioning of the chemistry scheme, two examples from ZDPlasKin are recreated.

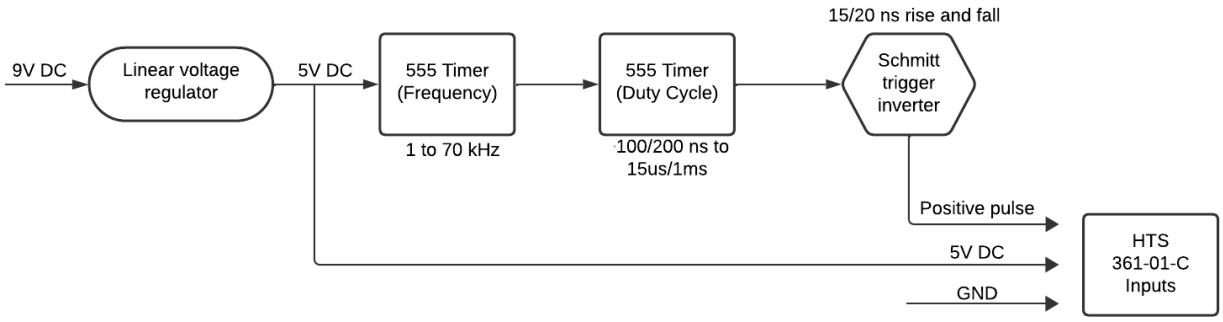

Figure 3.3 Block diagram for the control PCB of the Switch.

(a) Angle view of the proposed DBD reactor

(b) Front view of the proposed DBD reactor

Figure 3.4 DBD reactor 3D model.

3.2.1 Basic structure

The structure of the chemical reaction kinetics solver is shown in figure 3.5. Before the actual simulation, a chemistry reaction file needs to be created, that identifies the targeted species and their initial densities as well as the respective rate coefficient for each reaction.
Since Loki-B already supplies the rate coefficients of the electron impact-induced reactions for a given set of conditions and gas mixture, the integration of the chemistry scheme had to be implemented. The chemistry scheme addresses Loki-B to compute the rate coefficients of electronic reactions at a given time step. When the rate coefficients of all reactions are known, a set of coupled rate equations, following the notations given in ZDPlasKin 2.8, is solved. The new densities of each species are stored, as the electron density is supplied to

Loki-B for the next time step. When the desired duration of the simulation is reached, the densities are saved and the data is displayed.

3.2.2 Graphical user interface

To facilitate the use of this simulation tool, a graphical interface is proposed. In the form of a MATLAB application, the GUI allows the user to input basic conditions of the simulation such as the reduced electric field, the pressure, ambient temperature or duration. With this information, a text file is created which is later read by the master code, overriding some of the default parameters in Loki-B. The GUI also allows for the creation of a chemistry file. This feature aims to remove the tedious work of creating these text chemistry reactions files by hand. In other chemistry solvers, even a small deviation from the input format can stop the entire simulation. The chemistry file can then be created with the exact intended reading format of functions utilizing this information. The main GUI window can also launch the simulation with a specified chemistry, condition and cross-section files.

3.3 $O_2(^1\Delta_g)$ and ozone detection

3.3.1 Macro Atmospheric Pressure Plasma Jet

The plasma source used for this work study was a large capacitively APPJ as described in [39]. Basis of the jet are two rectangular stainless steel electrodes. They are 8 cm in length and 4 cm wide. Each electrode is 1 cm thick. Electrodes are positioned and fixed with a 2 mm gap between them. The sides of the electrodes are sealed with quartz panels and vacuum glue. The gas was fed between the electrodes by a conic gas adapter. Electrical excitation was delivered to the electrodes by RF type-N female coaxial connector. The bottom electrode was connected to the high voltage while the top one was grounded. The whole apparatus is kept together with polymer plates and screws which creates a manipulable support. The jet can be mounted on an optical post.

3.3.2 Power supply

For APPJ studies operated with RF power, a commercial power supply was used which consists of an RF excitation at 13.56 MHz. An initial sinusoidal voltage was created at 13.56 MHz by an arbitrary waveform generator (Siglent - SDG 2082X) at 300 mV peak to peak. This signal was fed to a class A, fixed gain, broadband power amplifier (Vectawave VBA400-110). The high voltage passed through a bidirectional coupler that acted as a

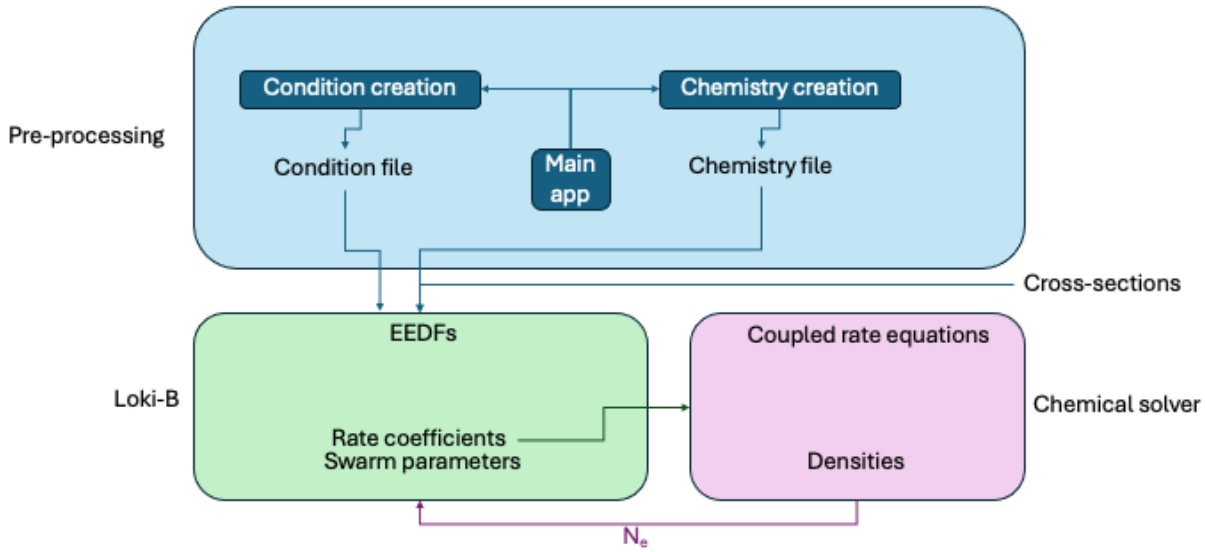

Figure 3.5 General structure for the chemical solver.

power meter (Monitor Sensors) which displayed the forward power and standing wave ratio. To match the impedance of the plasma source, a matching unit (Advanced Energy 5017-000-E) was inserted between the power meter and the APPJ. The used matching unit is simply two LC circuits (air copper coils and air variable capacitors), one in series and one in parallel with the load. The capacitor values were varied by a remote controller (Advanced Energy ATX-600) until the impedance was matched and the applied voltage to the electrodes was maximized. The amplitude of the applied voltage was controlled by the arbitrary waveform generator because the broadband amplifier has a fixed gain. The input voltage was gradually increased until breakdown to a glow discharge was achieved.

3.3.3 UV absorption of Ozone

To determine ozone density in the effluent of the APPJ, absorption in the UV around 254 nm was used. The effluent of the APPJ was collected by a glass adapter that converts the rectangular cross-section into a tube. The effluent was fed to a glass cell. On one side, a deuterium lamp (Ocean Insight DH 2000) was used as the broadband light excitation. Light was delivered by an optical fiber placed at the focal length of a lens so that the cell was uniformly illuminated. Before reaching the cell, the broadband light passed through a

narrow band-pass filter centered at 254 nm. After the cell, the light was focused on another optical fiber by a lens. The collected light was guided to a spectrometer (Ocean Insight USB2000+) and the spectrum was recorded via the software OceanView on a computer. The differences in intensity under different gas mixtures were converted to absolute densities by Beer-Lambert's law. Equation 3.4 was used to retrieve the density, where I_0 is the baseline intensity, I is the intensity when absorption is present, ϵ is the molar absorptivity, l is the absorption path and n the concentration.

$$\log_{10}\left(\frac{I_0}{I}\right) = \epsilon l n \tag{3.4}$$

A schematic of the proposed setup is shown in figure 3.6.

3.3.4 NIR emission of $O_2(^1\Delta_g)$

To determine $O_2(^1\Delta_g)$ density in the effluent of the APPJ, emission in the NIR was used. The effluent of the APPJ was collected by the same glass adapter used for the ozone measurements that converts the rectangular cross-section into a tube. Here, the effluent was fed into a calibrated glass cell with quartz windows. Light emitted from the $O_2(^1\Delta_g)$ transition to the triplet ground state was filtered by a narrow band-pass filter at 1270 nm (Andover 200FC39-25) before reaching an InGaAs photodiode (Judson model J22 D-M204-R03M-1.7). The detector converts the light into an electrical signal that is amplified by an in-house pre-amplifier. The amplified signal was read by an oscilloscope (Siglent SDS3104X) in averaging mode. This measured voltage can be correlated to an absolute density of $O_2(^1\Delta_g)$ with a conversion factor. To reach this conversion factor, the authors of [27] first performed a ray-tracing Monte-Carlo simulation, taking into account the cell dimensions, reflection probability of photons on cell walls and windows, which ultimately gave the probability of an emitted photon in the detection cell to reach the detector. Then, assuming uniform density of $O_2(^1\Delta_g)$ in the cell and taking into account the filter transmission, the efficiency of the InGaAs photodiode and the pre-amplifier gain, the conversion factor of $3.7 * 10^{15}$ molecules/cm^3 per mV is obtained, leading to calibration of the detection cell [27]. This exact detection setup is used in this thesis. The voltages associated to different gas mixtures were then converted to absolute densities. A schematic of the proposed setup is shown in figure 3.7.

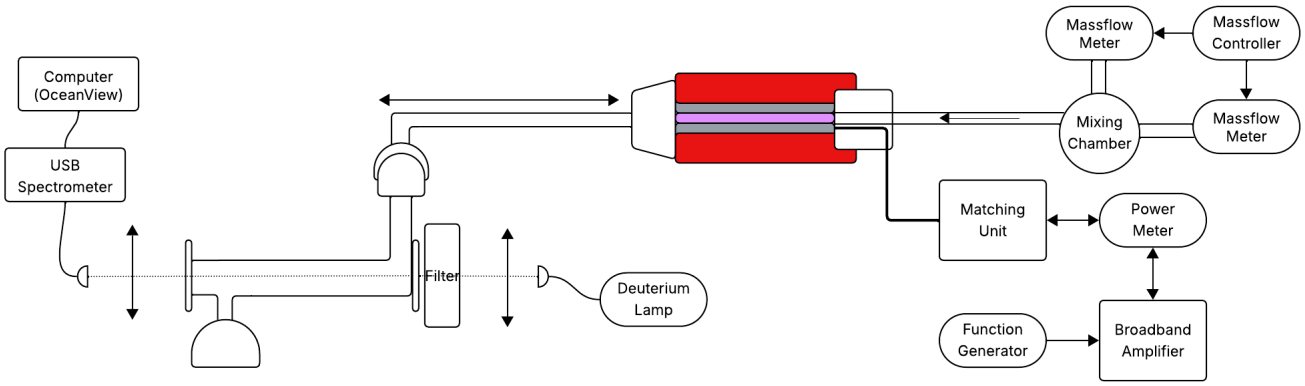

Figure 3.6 Ozone absorption setup in the effluent of an APPJ.

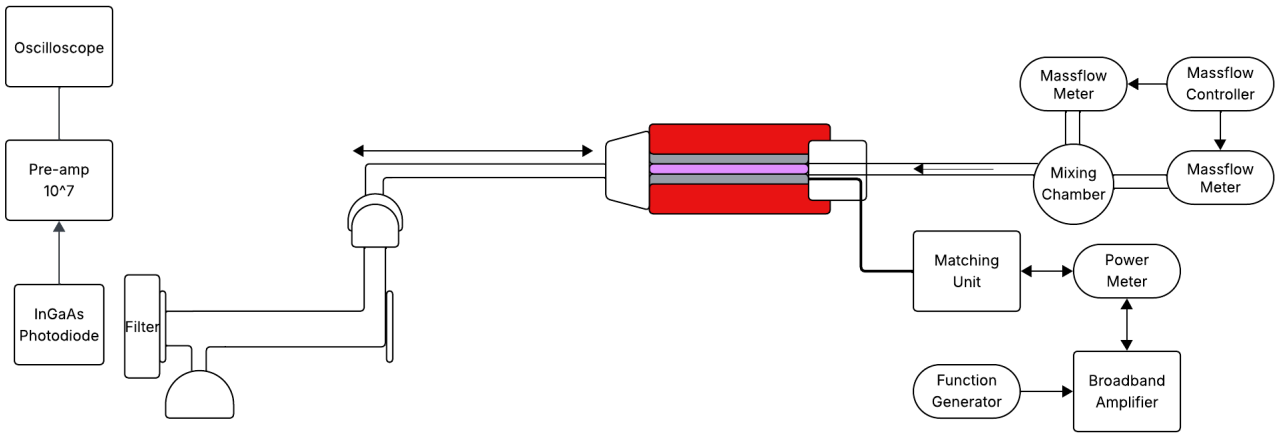

Figure 3.7 $O_2(^1\Delta_g)$ emission setup in the effluent of an APPJ.

CHAPTER 4 THEORETICAL AND EXPERIMENTAL RESULTS

In this chapter the results for the the high voltage electric pulser, ozone measurements, $O_2(^1\Delta_g)$ measurements and modeling are presented.

4.1 Pulse power supply

First, the results are shown for the CW generator with an open load. Secondly, the pulse forming circuit is presented as well as the plasma reactor. Afterwards, the results of all the parts together are shown, as well as the adjustments required for their integration.

4.1.1 CW generator

The power is obtained from the wall outlet and passed through an isolation transformer to create an independent ground. A variable transformer then modulates the amplitude of the sine wave at 60 Hz from 0 to 394 V peak to peak. The voltages measured from this section are read by a high voltage probe (Cal-Test Electronics CT4028) and onto which data is saved in CSV format. A Python code later reads the data and plots the results shown in this section. Now that the power input is successfully created and adjustable, it is connected to a 10 stages CW generator. Figure 4.1 shows an example of a multiplication card with 10 stages. The input signal is connected to the card by the green and white wire, the white wire being the ground in this example. Each stage is composed of two 400 V rated 22 μF capacitors, two fast diodes, and a ring connector. This ring connector plays two roles: it allows one to measure the voltage at the output of each stage, and when testing is completed and the variable transformer removed from the setup, it allows one to control the DC high voltage amplitude.

To ensure proper operation of the card, the AC input voltage is gradually increased while the amplified DC voltage is monitored. Without load, the card should follow the trend expected by equation 3.1, where n equals 10. The results of the output voltage measured after the 10th stage as a function of the input peak voltage are shown in figure 4.2. The theory is also closely followed when the input voltage is kept constant but the voltage is measured at each stage, as seen in figure 4.3. These multiplication cards, based on the schematic presented in figure 3.1, each containing 10 stages can be stacked and connected in series to provide an even higher output voltage. Figure 4.4 shows two multiplication cards connected in series. The cards are separated and mounted with nylon spacers, ensuring enough space and isolation.

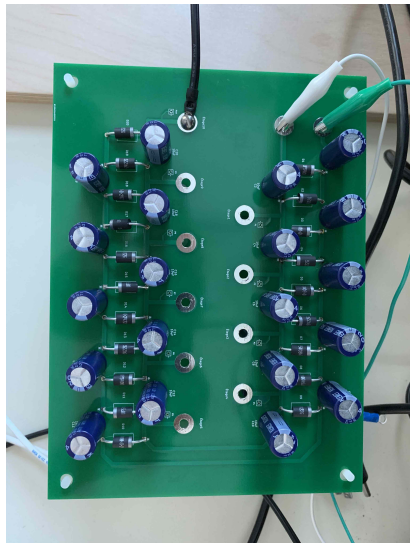

Figure 4.1 Multiplication card of the CW generator.

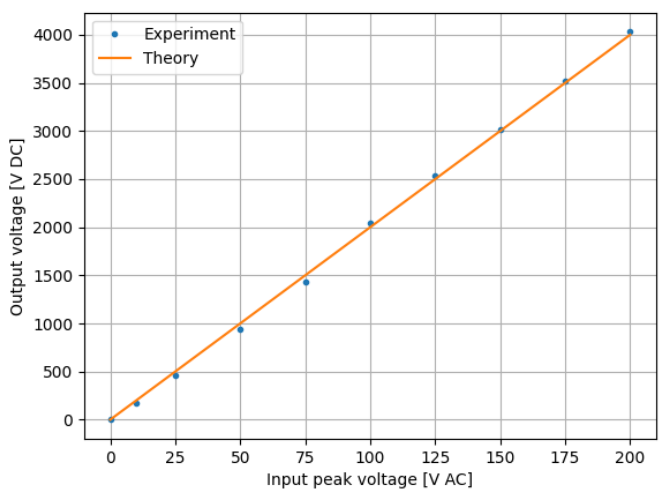

Figure 4.2 Output voltage at stage 10 as a function of the input peak voltage for an open circuit load.

The input voltage is kept constant (at its maximum) and the voltage is measured at each stage for an open circuit load but this time with two cards, the CW again closely follows theory. However, as seen in figure 4.5, there is some loss in the CW generator as the number of stages increases. The CW generator can provide close to 8 kV DC with two cards. The complete list of the components and their respective cost is included in annex A. The total cost of this HV DC power supply is estimated to 340$.

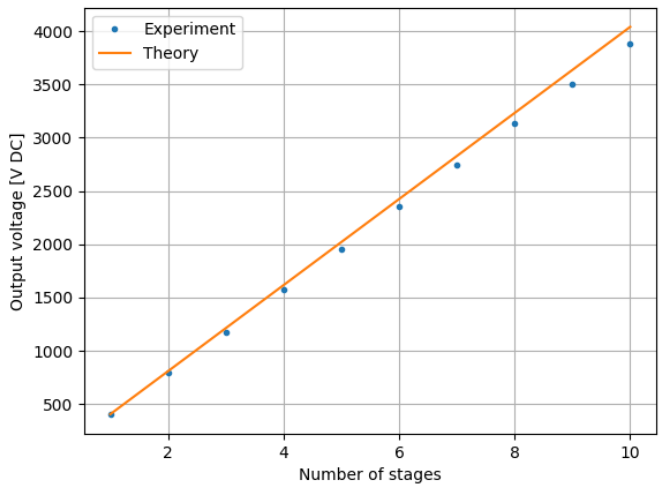

Figure 4.3 Output voltage at each stage with maximum input peak voltage for an open circuit load.

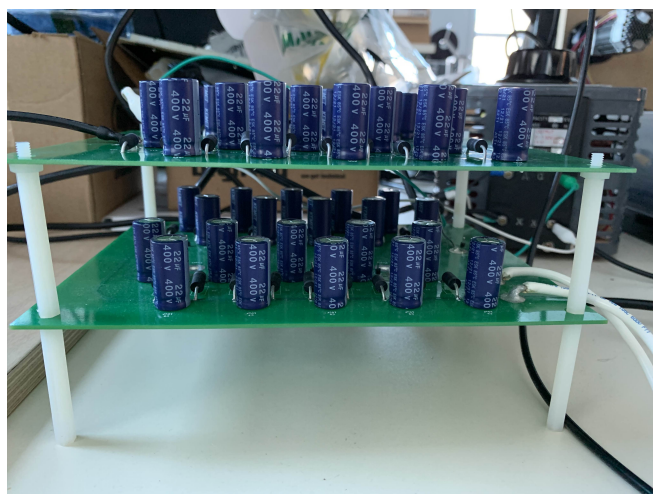

Figure 4.4 Two multiplication cards of the CW generator.

4.1.2 MOSFET switching circuit

The switching circuit is based around the HTS 361-01 MOSFET switch from BEHLKE. The main input is the HV DC taken from the CW generator and the main output is the high voltage pulse train. The resistors and capacitors connected to the high voltage DC terminal or to the electrodes must be rated properly, adding complexity to the circuit. The circuit chosen for testing is the one recommended by BEHLKE. A CAD model was made in the Fusion 360 program to organize the physical layout. The model replicates the schematic shown in figure

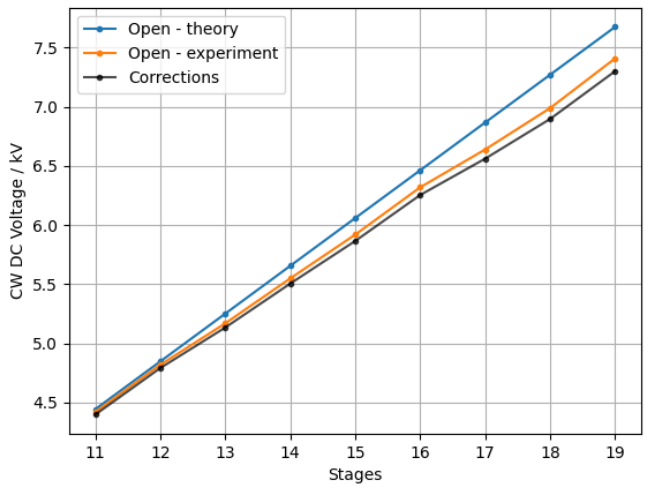

Figure 4.5 Output voltage at each stage with maximum input peak voltage for an open load with 2 cards.

3.2. The layout of the pulsing circuit is shown in figure 4.6, where the orange wire is the high voltage DC that comes from the CW generator, the purple wire is the HV pulses going to the DBD reactor, and the black wire is a ground connection. The resistors used in this

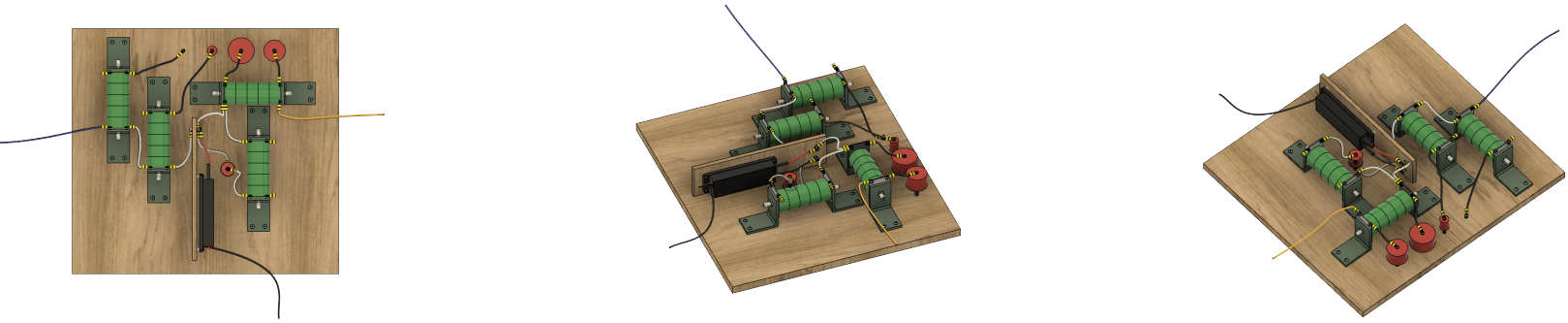

Figure 4.6 3D model of the physical layout for the pulsing circuit.

work are self-assembled. The green disks are high voltage resistors with low inductance. These disks are stacked and sandwiched between two metal plates, each with two holes to provide placement of electrical connections. The supports are made from glass fiber. All the components and are compressed by a nylon rod and bolts. This modular assembly is excellently suited for testing. The ideal resistor values are determined empirically and they are changed by adding or removing disks. To ensure concentricity, 3D printed supports are placed under the disks while clamping them. A 3D model of a resistor is shown in figure 4.7

The actual physical layout of the pulsing circuit (including the CW generator) is shown in

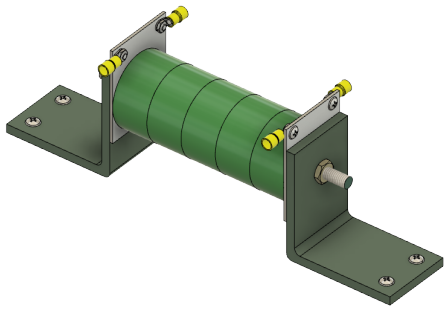

Figure 4.7 3D model of a high voltage resistor with low inductance.

figure 4.8, as well as the DBD reactor. A cage was built around the DBD reactor with a gas exhaust to extract any dangerous gaseous species created by air discharges, notably ozone.

The control circuit that provides the 5 V DC auxiliary power and the TTL is shown in

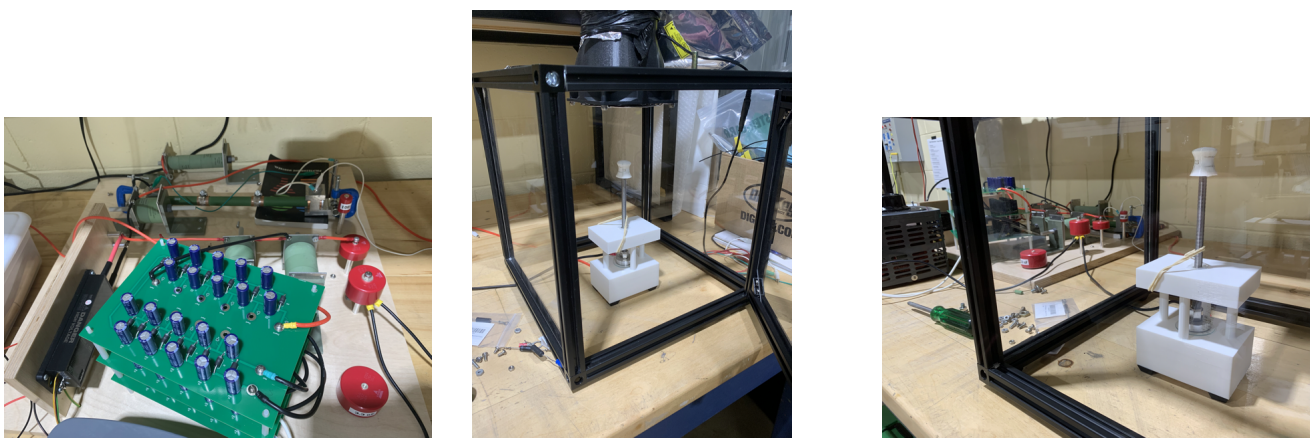

Figure 4.8 Physical layout of the pulser with the DBD reactor.

figure 4.9. The user changes the value of the two potentiometers to change the frequency and duty cycle of the TTL. The jumper wires are set manually to choose different frequency ranges.

4.1.3 End-to-end solution

After a high voltage DC was created and a controlled pulse reached the DBD reactor, plasma breakdown was attempted. The voltage waveform was measured at the output of the switch.

Figure 4.9 3D model of the control PCB for the Behlke switch.

A 7.5 kV amplitude pulse with a 500 ns pulse width at 2 kHz repetition frequency was sent, but no breakdown was observed. The reason for this that the pulses were discharged in the R_L load resistor in parallel to the plasma load. The current passing through was too high and a voltage drop was induced in the CW generator as predicted by equation 3.3, because a load was now connected to it. This rapid drop, (around 1 s) reduced the applied voltage at the electrodes below the breakdown voltage. The voltage drop of the CW generator was monitored at different stages with a constant input voltage for different R_L values. Results are shown in figure 4.10. The voltage drop is extremely significant, nearing 50% with an R_L value of 5.4 kΩ at 19 stages. The higher the resistor value, the less current passed at each pulse, which resulted in a smaller voltage decrease. To bring the output voltage of the CW generator closer to the open circuit condition and have a sufficiently high voltage to induce plasma breakdown, we again look at equation 3.3. Which indicates the relevant role of the input frequency of the CW.

To resolve the issue, instead of the 60 Hz from the wall outlet, a higher frequency signal was used as input. A function generator was used to send a 0 to 20 V peak to peak from 60 Hz to 10 kHz to a broadband power amplifier. The amplified signal was used as input to the CW generator. This change in frequency greatly helped reduce the voltage drop from the CW generator. For a purely resistive load of 72.3 kΩ (R_L with disconnected from the plasma reactor), figure 4.11 shows the gain in output voltage of the CW generator as a function of its input frequency for three arbitrary input amplitudes. The amplitudes of the input sinusoidal signal were modulated with the VARIAC placed at 20, 50 and 80 % position. The number of stages in the CW generator was 25 while the pulse repetition frequency was 4.4 kHz and the pulse width was 4.2 μs. It is clear that 1 kHz as the input frequency was enough to limit the voltage loss to an acceptable value, regardless of the input amplitude. In what follows,

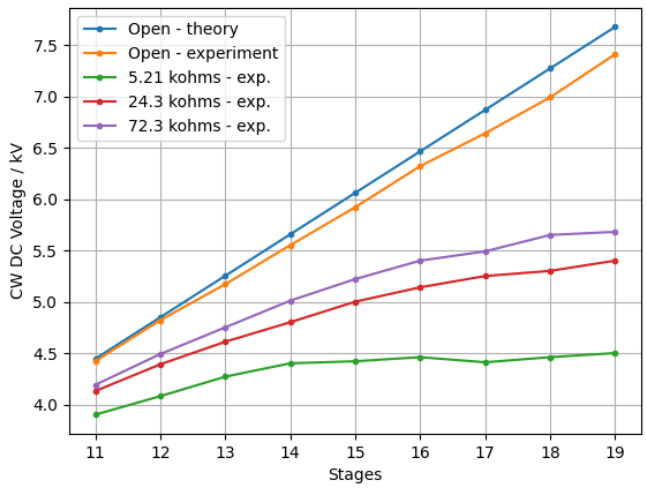

Figure 4.10 Output of the CW generator with different loads as a function of stages.

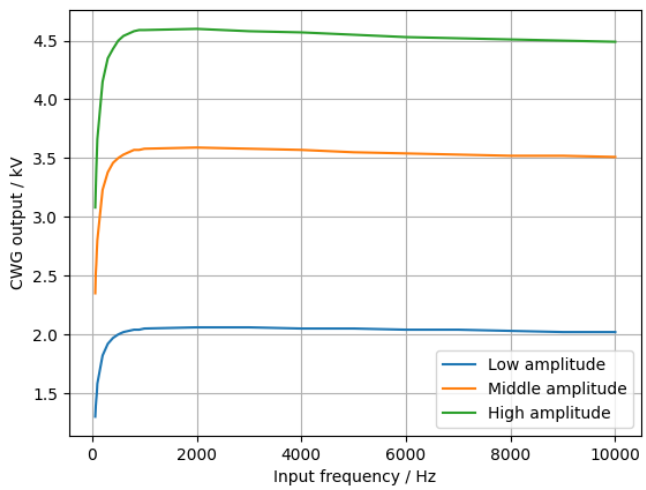

Figure 4.11 CW output voltage for a 72.3 kΩ load for three input amplitudes.

for the same load, an output pulse characterization was performed. Using the control circuit and the variable transformer, pulses with different amplitudes are shown in figure 4.12, duty cycles in figure 4.13, and repetition frequencies in figure 4.14.

Figure 4.15 shows the very fast rise time of around 40 ns and the longer fall time. This long tail is attributed to the nature of the load and the intrinsic capacitance of the switch, which is between 30 to 300 pF. Together, they create an RC circuit that discharges with a time constant proportional to the resistance value. This long trailing edge is not desired and ways

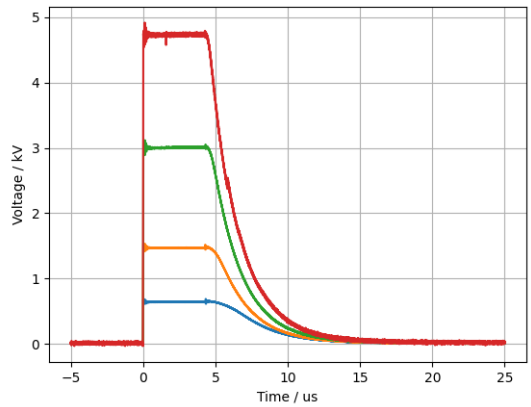

Figure 4.12 Different amplitudes with a 72.3 kΩ load.

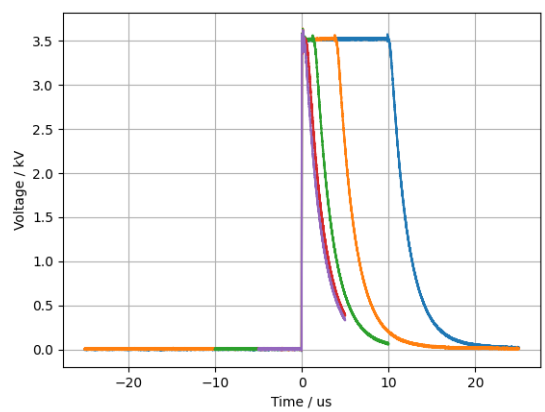

Figure 4.13 Different duty cycles with a 72.3 kΩ load.

to circumvent that are discussed later in this thesis.

Finally, the DBD reactor was reconnected in parallel with the R_L resistor of 72.3 kΩ and an air plasma was ignited between the dielectric and the grounded electrode. The gap was approximately 0.5 mm. The discharge is seen in figure 4.16.

4.2 O_3 and $O_2(^1\Delta_g)$ measurements with RF excitation

The power was brought to the APPJ by a coaxial cable terminated with a type-N connector. The high voltage part was connected by an exposed copper wire to the bottom electrode. The high voltage probe (Cal-Test CT4028) was anchored to the exposed wire with its fish hook adapter. The high voltage probe slightly changed the matching circuit and so it was left

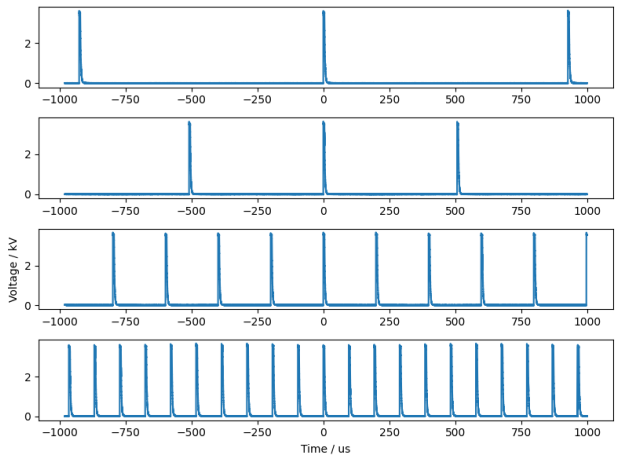

Figure 4.14 Different frequencies with a 72.3 kΩ load.

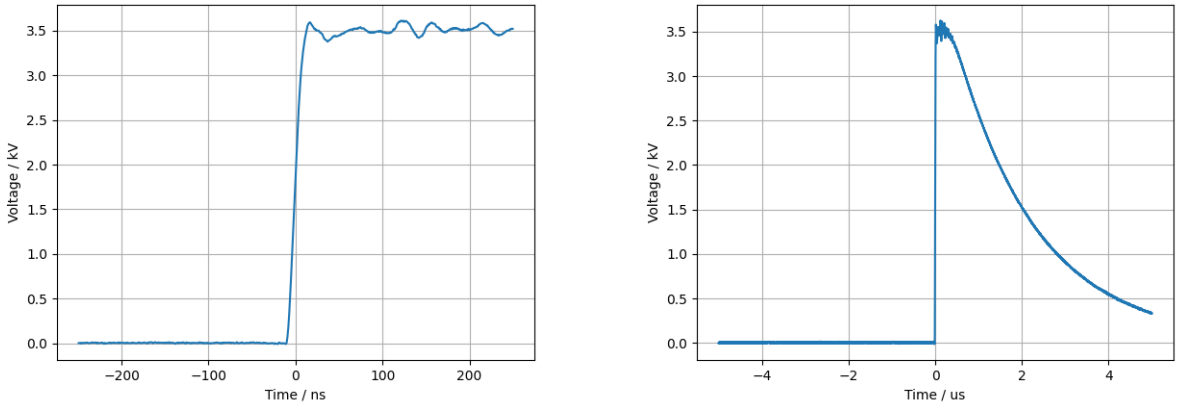

Figure 4.15 Voltage rise and complete pulse waveform for a 72.3 kΩ load.

in place for all measurements. A Faraday cage was constructed around the APPJ as the RF excited plasma acts as an antenna. The electromagnetic noise induced by the plasma can be picked up by the oscilloscope, the probes or other equipment in the laboratory. Composed of aluminum extrusion and a fine copper mesh, the grounded cage reduced electromagnetic noise. The cage and the high-voltage probe as well as the APPJ and its glass adapter can be seen in figure 4.17. The oxygen gas was taken from the central gas line and brought to the experimental setup by approximately 10 m of PTFE tubing. The helium was taken from a bottle and brought to the experimental setup by approximately 3 m of PTFE tubing. The flow of each gas was controlled by mass flows (MKS) with 10 SLM and 100 SCCM range for helium and oxygen respectively. The flow was adjusted by a mass flow controller (MKS 647C). After passing through their respective mass flow controller, the gases were

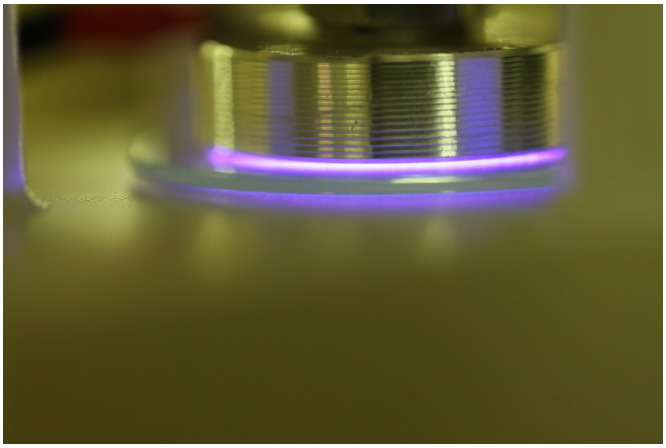

Figure 4.16 Air discharge in the DBD reactor from a pulse excitation.

Figure 4.17 APPJ and collector adapter with a He gas mixture.

mixed in a mixing chamber to ensure gas uniformity. The gas mixture was then fed to the APPJ by a 1 m PTFE tube. The gas connections were made with quarter inch Swagelok connectors. The mixing chamber, constructed by Joël Bouchard is shown in figure 4.18.

Figures 4.19 and 4.20 are close-up of the APPJ and were respectively created by RF signals at 13.56 MHz and 35 W forward power and 5 SLM total flow in pure helium and He:O_2 0.99:0.01 mixture. When oxygen was added to the gas mixture, the plasma color changes from pink to white.

To qualitatively assess impurities in the gas mixture, emission spectra were taken from the plasma bulk. An optical fiber was placed 2 cm from the plasma bulk and connected to a USB spectrometer (Ocean Insight USB2000+). The placement of the optical fiber relative to the APPJ is shown in figure 4.21. Spectra were treated and saved via a computer. The power was kept constant at 35 W and the total flow was 5 SLM. As seen in figure 4.22, a lot

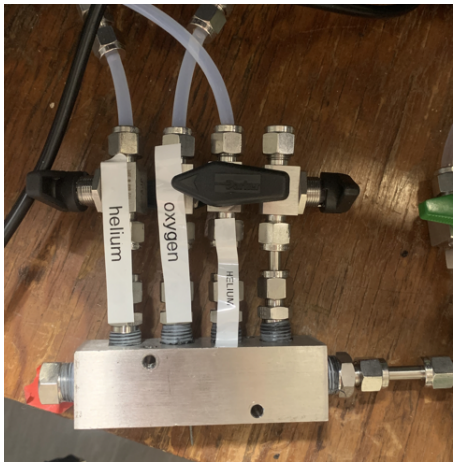

Figure 4.18 Mixing chamber for helium and molecular oxygen.

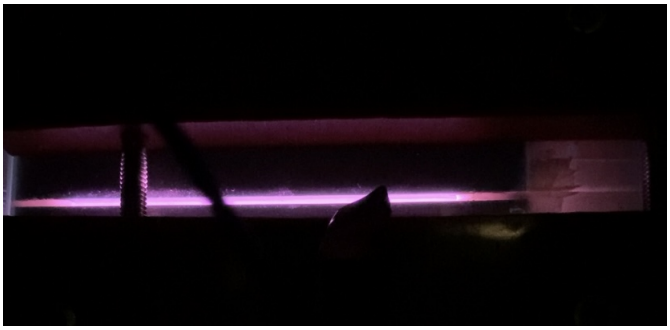

Figure 4.19 Discharge of the APPJ in pure Helium.

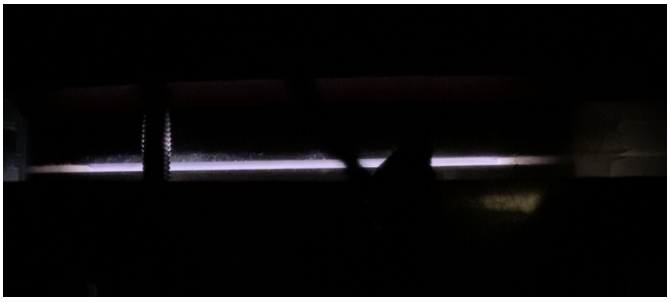

Figure 4.20 Discharge of the APPJ in He:O_2 0.99:0.01 admixture.

of impurities were present at the beginning. It was expected as it takes some time to clear the gas lines from ambient air. Nitrogen, oxygen and hydrogen based emission were observed at the start, and they gradually decreased as time passed. However, even after 27 minutes some impurities remained. These impurities do not gravely affect the chemistry as discussed further in this section. In order to demonstrate the dependence of the emission signals on

Figure 4.21 Bulk emission setup for the APPJ.

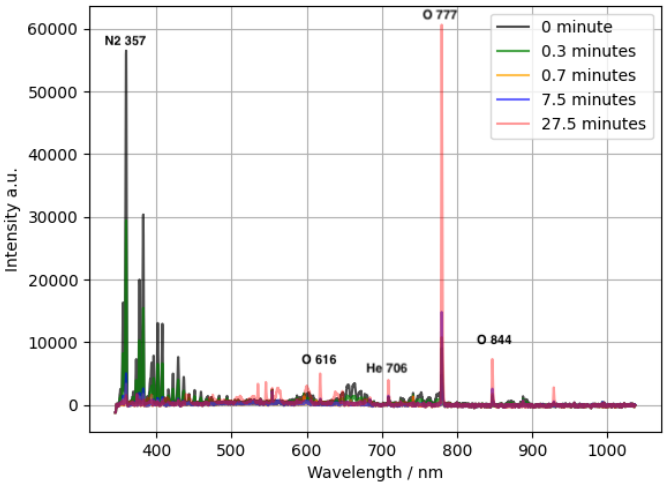

Figure 4.22 Emission spectra from the bulk plasma of the APPJ in He:O_2 0.99:0.01 admixture.

the impurity levels under varying admixture conditions, the same setup, as described above, was used next to follow the intensity of the principal emission lines. Results are shown in figure 4.23. At the top of figure 4.23, percentage of molecular oxygen in the feed gas is shown in red while the total flow was kept at 5 SLM and with a 35 W forward power. The vertical black lines represent a change in the He:O_2 admixture. Letters are introduced to facilitate the explanation of the emission over time. Time **A** marks the debut of the experiment in pure helium. From **A** to **B** is the time required to stabilize the power to 35 W. Emission of atomic oxygen slowly increases over time between **B** and **C** as the He gas line and APPJ clear from impurities, notably humidity. The emission of atomic oxygen sharply rises from **C** to **D** probably due to the removal of most of the humidity and nitrogen species, known scavengers of atomic oxygen. Shortly after the point **D**, molecular oxygen was introduced in the feed gas

at a concentration of 0.1%. Emission rapidly decreased and more or less stabilized between **E** and **F**. Afterwards, each time the O_2 content was increased, overall emission went down as seen between **H** and **I**. With more molecular oxygen, the plasma becomes less efficient and emission goes down. At point **J** the O_2 content in the feed gas is shutoff. Emission rapidly increased as the plasma became more efficient and traces of O_2 were still present in the mixing chamber and the gas line. The emission reached the starting value of pure helium at point **M** after a 5 minutes wait. Four main takeaways were identified from this experiment. First, a waiting time at the start with both gases flowing is essential as the plasma isn't stable. This waiting period is set at 10 minutes. Second, the plasma stabilizes very quickly when increasing the O_2 content in the admixture. The waiting period before acquiring data when O_2 is increased is set at 1 minute. Third, the plasma takes a long time to stabilize when the O_2 content in the admixture is decreased. The waiting period before acquiring data when O_2 is decreased is set at 5 minutes. These three waiting times were incorporated for later experiments. Finally, base O_2 impurities in the feed gas were estimated below 0.1%.

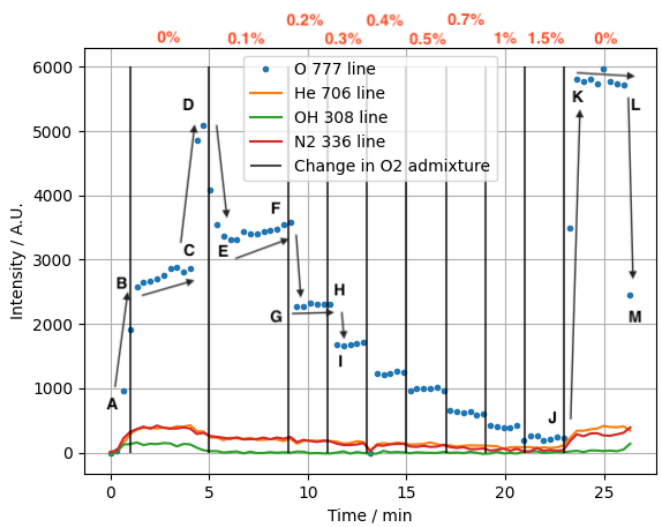

Figure 4.23 Evolution of the principal emission lines from the bulk plasma of the APPJ with different O_2 admixture.

4.2.1 Ozone

The ozone density, obtained from Beer-Lambert's law as described in section 3.3.3, was first investigated over time at fixed plasma conditions. The optical setup, schematized in figure 3.6, comprised of two optical fiber holders, two lens, a narrow band filter and a glass cell, used for UV absorption is shown in figure 4.24. The effluent of the APPJ was simply passed

through the detection cell by one of the inlet. To ensure proper alignment, the detected signal at 254 nm was maximized before taking data. For a 35 W forward power plasma, 1%

Figure 4.24 Optical setup for ozone absorption.

O_2 admixture and 7.5 SLM total flow, ozone density evolution over time is presented in figure 4.25. A spectrum was registered every 20 seconds. The ozone density seemed to stabilize in the first 5 minutes before quickly increasing. This sharp increase was attributed to the humidity disappearing from the gas lines. In fact, the distance from the central oxygen gas line to the mixing chamber is around 10 m in PTFE tube. Water, a known scavenger for ozone, diminished the ozone density in the effluent for the first 7 minutes. After reaching a maximum, the ozone density decreased slowly. This is attributed to thermal effects. Over time, the whole reactor heated up due to the heat from the discharge. A thermocouple was placed on the outside polymer of the reactor and the registered temperature went from room temperature to 70 °C. The electrode temperature is assumed to vary by a lot more, enough to explain the ozone instability. The small spikes were from the constant adjustments of the input signal from the waveform generator to maintain 35 W of forward power. For more stable operation, the APPJ could be water cooled.

The results for ozone density in the effluent of the atmospheric pressure plasma jet obtained by varying oxygen content of two different total flow are shown in figure 4.26. The forward power was kept constant at 35 W. It is assumed that the power, the basis for comparison,

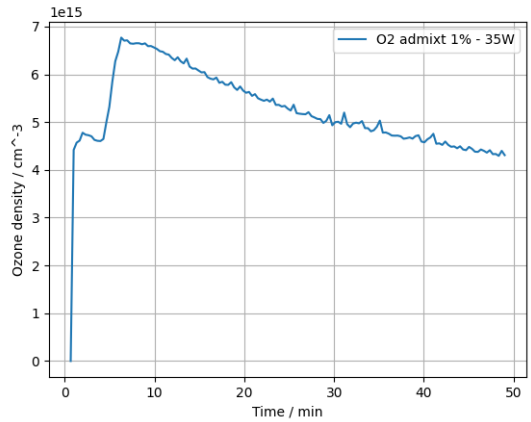

Figure 4.25 Evolution of the detected O_3 density over time for fixed conditions.

stays constant but the true power dissipated in the plasma might not be kept constant as discussed in section 5.2. The zero values for the Beer-Lambert calculations were taken at no plasma conditions and the pure helium condition is the first data point on the figure. Because no ozone was detected in pure helium, the gas impurities are assumed sufficiently low to have no influence on the results. As expected, ozone densities increased with the O_2 content in the gas mixture. Also, a higher total flow yielded more ozone (by a little more then a factor 2). The error bars are calculated from the variance in intensity of the registered spectra. The detection limit was set to $4.0 * 10^{14}$ molecules/cm^3, where the error bars are within the same range as the measured densities.

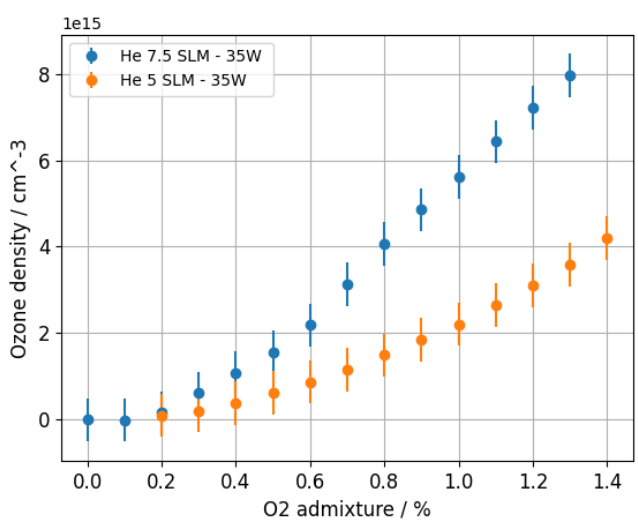

Figure 4.26 Ozone density for different flow conditions and He/O2 admixtures.

4.2.2 $O_2(^1\Delta_g)$

The setup for $O_2(^1\Delta_g)$ detection, schematized in figure 3.7, is presented in figure 4.27 and 4.28. Figure 4.27a shows the APPJ, the glass adapter and its holder. They were clamped together using C-clamps, themselves supported by 3D printed supports, an adhesive foam for the coupling and a 3D printed plaque. This ensured good coupling between the APPJ and the glass adapter, limiting impurities. The glass adapter was connected to the glass cell (shown in figure 4.27b) by a metal clamp. On the other side of the calibrated cell the detector

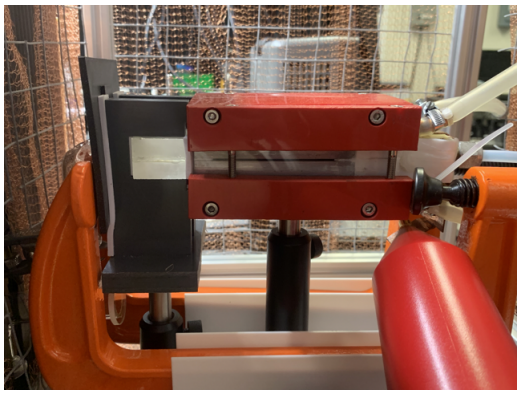

(a) Clamped APPJ and glass adapter

(b) Close-up side view of the calibrated cell between the glass adapter and detector

Figure 4.27 $O_2(^1\Delta_g)$ detection setup: APPJ and glassware.

was positioned at the center of the quartz window. The detector and the pre-amplifier are shown in figure 4.28. The detector and pre-amplifier were wrapped in aluminum foil to limit electromagnetic interference. They were encapsulated in a metal box for the same reason. This box also shielded most of the parasitic light. The voltages of the photodiode signal of the $O_2(^1\Delta_g)$ detection system were measured by the oscilloscope after the pre-amplifier and were done in averaging mode. The averaging was set to 1024 and the time scale to 1 ms per division. If too much noise was still present, frequencies from 13 to 14 MHz were filtered by the oscilloscope. As for the ozone measurement, a stability curve was constructed for fixed plasma conditions. The forward power was kept at 35 W, total flow of 5 SLM with an admixture of 0.2% O_2 and a measurement distance of 250 mm. The gain of the amplifier was set at 10^7. The measurement distance was defined as the distance between the end of the electrodes and the center of the calibrated cell. The measured signals are shown in figure 4.29. The $O_2(^1\Delta_g)$ signal was relatively stable but decreased slightly over time. Figure 4.30 represents the measured voltages for different oxygen admixtures of two different powers and measurement distances. Again, the total flow of helium was kept constant at 5 SLM. For

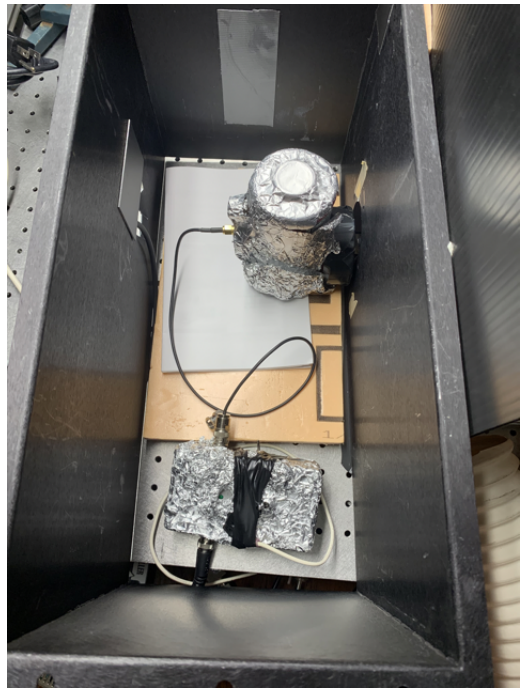

Figure 4.28 $O_2(^1\Delta_g)$ detection setup: detector and signal pre-amplifier.

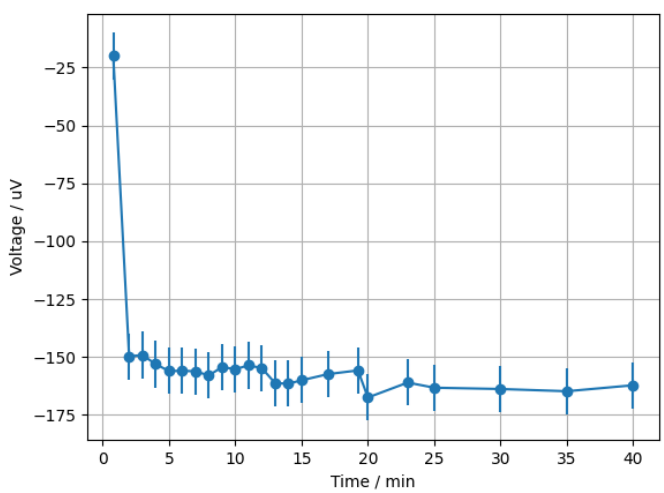

Figure 4.29 Evolution of the detected voltage over time for fixed conditions.

all tested conditions, the measured voltage decreased sharply before reaching a minimum at 0.1 % of O_2 content. The voltage then increased towards the initial value. At 1 % admixture, voltages are comparable to pure helium signals. Higher power yielded lower voltages and a closer measurement distance (140 instead of 250 mm) also gave lower voltages.

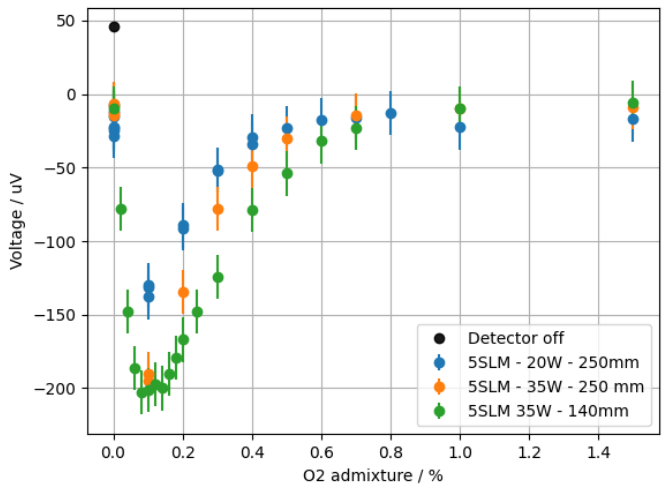

Figure 4.30 Comparison of the detected voltages for different powers and detection distance.

After using the conversion factor of $3.7 * 10^{15}$ molecules/cm^3 per mV for this calibrated cell [27], which is obtained by a previously performed ray-tracing Monte-Carlo simulation, voltages were expressed as absolute densities in the calibrated cell. Figure 4.31 shows the density dependencies on total flow, power, measurement distance and O_2 content. Again, it is assumed that the power, the basis for comparison, stays constant but the true power dissipated in the plasma might not, as discussed in section 5.2. The error bars are only shown on one measurement for visualization purposes. These error bars were calculated from the statistical variance of the detected voltages. The detection limit is set to $1.0 * 10^{14}$ molecules/cm^3 since the densities are within the same range as the error bars. Multiple dependencies can be interpreted from this graph. More power yielded more $O_2(^1\Delta_g)$. A higher total flow or smaller detection distance, both associated to a shorter time of flight of species in the effluent, also yielded a higher $O_2(^1\Delta_g)$ density. As the time of flight decreased, the maximum $O_2(^1\Delta_g)$ density shifted towards higher O_2 admixture.

4.3 Plasma kinetics modeling

In what follows, results from the kinetics model are described. The main GUI page obtained from running the MATLAB application is shown in figure 4.32. From this window, simulation was launched or the window for either the chemistry or condition text files creation were opened. File creation interfaces are shown in figure 4.33 and 4.34, respectively.

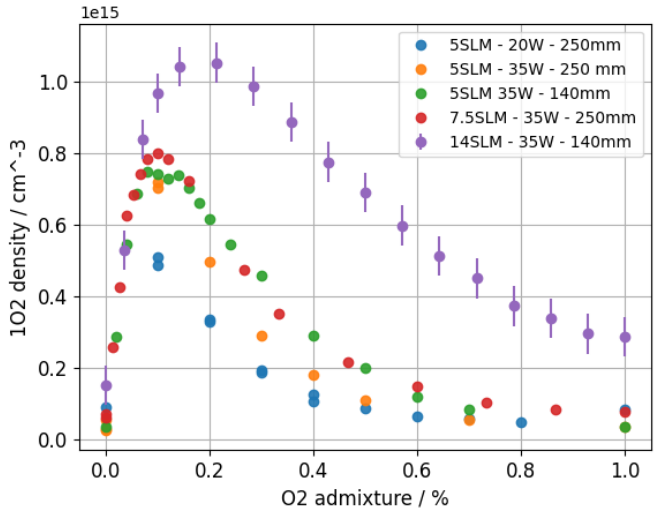

Figure 4.31 Comparison of $O_2(^1\Delta_g)$ density for different total flows, powers and measurement distances.

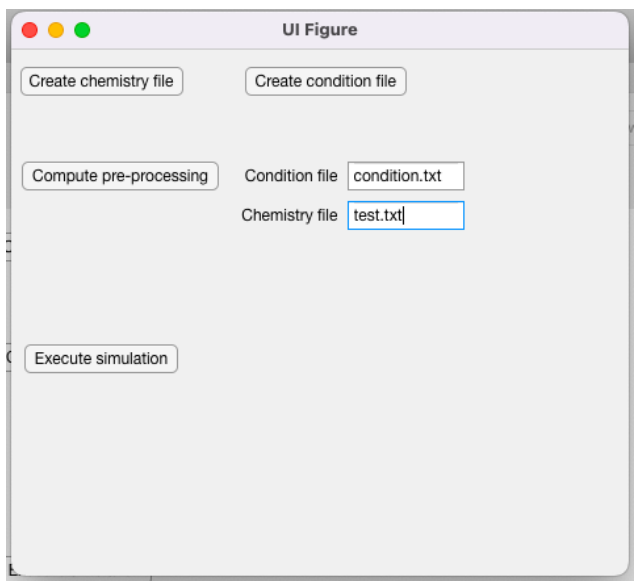

Figure 4.32 GUI main window.

The first example available on the ZDPlasKin website was recreated. It is a simple test case of two reactions in an argon plasma with a constant reduced electric field of 50 Td. Simulation was carried out using the ZDPlasKin tool (Bolsig+) and compared to the newly developed chemical kinetics solver that implements Loki-B as the Boltzmann solver. The reactions considered for this example are described in table 4.1. Where $f(e)$ is the rate of reaction 1 obtained by either Bolsig+ or Loki-B. The results for the electron density evolution over time

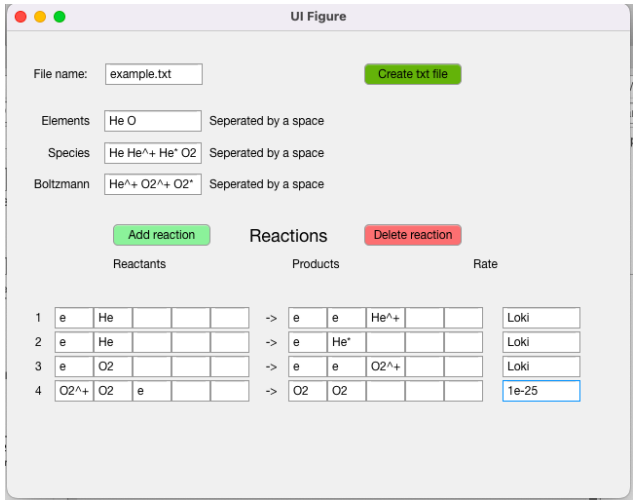

Figure 4.33 GUI for the creation of the reaction set file.

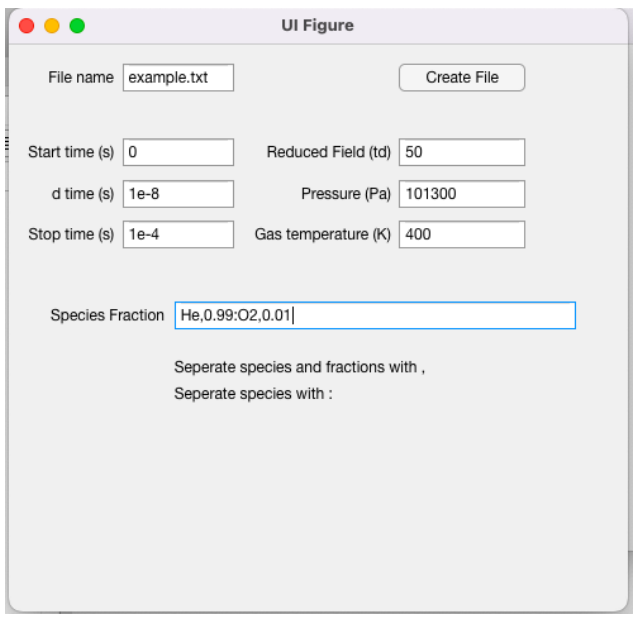

Figure 4.34 GUI for the creation of the condition file.

Table 4.1 Zdplaskin's 1st example reactions.

#	Reaction	Rate
1	$e + Ar \rightarrow e + e + Ar^+$	$f(e)$
2	$e + Ar^+ + Ar \rightarrow Ar + Ar$	$10^{-25} cm^6/s$

obtained from the two tools are presented in figure 4.35. Solid lines represent the custom solver, while crosses are results from ZDPlasKin The electron density is in excellent agreement

with ZDPlasKin. Argon ions density is not shown here for a visualization perspective, as they follow exactly the density of electrons. This simple test case demonstrated the basic operation of the new chemical kinetics solver.

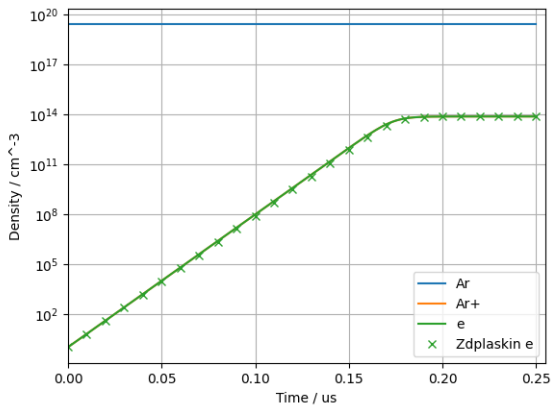

Figure 4.35 Electron density comparison for the first example between ZDPlasKin and the in-house tool.

The second example from ZDPlasKin's website is recreated as well. This example is more complex, taking into account more reactions. However, the complexity arises from the non-uniform character of the reduced field. ZDPlasKin allows the user to provide code in Fortran 90 to include more complex behavior in the discharge region. As a matter of fact, when a discharge is induced by a high enough reduced field, the gas becomes conducting and the voltage subsequently drops. This example aims to model such behavior and the impact it has on the species densities by replacing the plasma with an equivalent circuit. At first, this example was created to validate experimental results of a macro-cathode discharge, so experimental geometric parameters are also taken into account. The reactions considered are presented in table 4.2. The plasma is simply considered as a 100 kΩ resistor with a constant applied voltage of 1000 V. At each time step, a current density is calculated with the geometric parameters and the electron drift velocity. Over that resistor this current infers a new voltage which over the discharge region distance, gives a new reduced field. Rate coefficients are calculated with this new reduced field. It is worth mentioning that the Boltzmann equation is solved at each time step with the assumption of a uniform electric field. Although this approximation might lead to inaccurate densities, the same code was implemented to show that our chemical tool provides the same flexibility. The results of the densities from the two simulation tools, as well as the electric field are compared in figure

4.36. Again, the results were very similar validating the good implementation of our chemical tool.

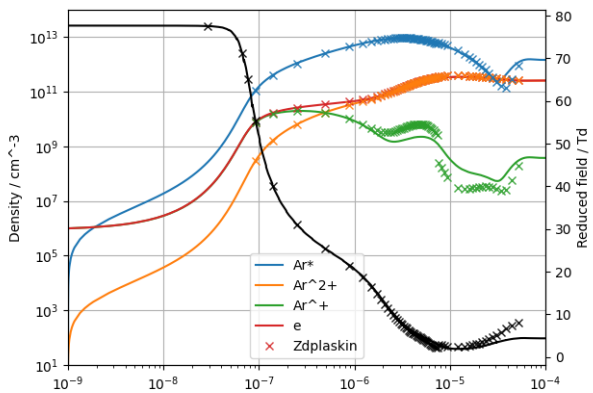

Figure 4.36 Species density and reduced field comparison for the second example between ZDplaskin and the in-house tool.

Finally, a first approach to modeling an arbitrary chemistry model was attempted. Now that the chemical tool and the link to Loki-B was validated, a more complex He/O2 model was taken from literature [1], as it is the gas mixture of interest. This model was composed of 108 reactions involving 19 species. The reaction set is presented in annex B. To recreate the plasma conditions of interest while detecting $O_2(^1\Delta_g)$, the frequency was set to 13.56 Mhz, while the pressure was set at 101 kPa and temperature at 400 K. The amplitude of the reduced field was approximated to 25 Td and is used here. The densities results are shown in figure 4.37. Unfortunately, at the time, the model does not converge as the density of oxygen-excited species, notably $O_2(^1\Delta_g)$, keeps increasing and does not reach equilibrium. In addition, to achieve this result, electrons are artificially removed at an arbitrarily chosen rate to ensure that equilibrium is reached for He^+ and O_2^+.

Table 4.2 ZDPlasKin's second example reaction set.

#	Reaction	Rate
1	$e + Ar \rightarrow e + e + Ar$	f(e)
2	$e + Ar \rightarrow e + Ar^*$	f(e)
3	$e + Ar^* \leftarrow e + Ar$	f(e)
4	$e + Ar^* \rightarrow e + e + Ar^+$	f(e)
5	$e + Ar_2^+ \rightarrow Ar + Ar^*$	$8.5^{-7}\left(\frac{11600T_e}{300}\right)^{-0.67}$
6	$Ar_2^+ + Ar \rightarrow Ar + Ar + Ar^+$	$\frac{6.06e-6}{T_{gas}}e^{-\frac{15130}{T_{gas}}}$
7	$Ar^* + Ar^* \rightarrow e + Ar_2^+$	6.0e-10
8	$Ar^+ + e + e \rightarrow e + Ar$	$8.75e-27(\frac{11600T_e}{300})^{-4.5}$
9	$Ar^* + Ar + Ar \rightarrow Ar + Ar + Ar$	1.4e-32
10	$Ar^+ + Ar + Ar \rightarrow Ar_2^+ + Ar$	$2.25e-31(\frac{T_{gas}}{300})^{-0.4}$

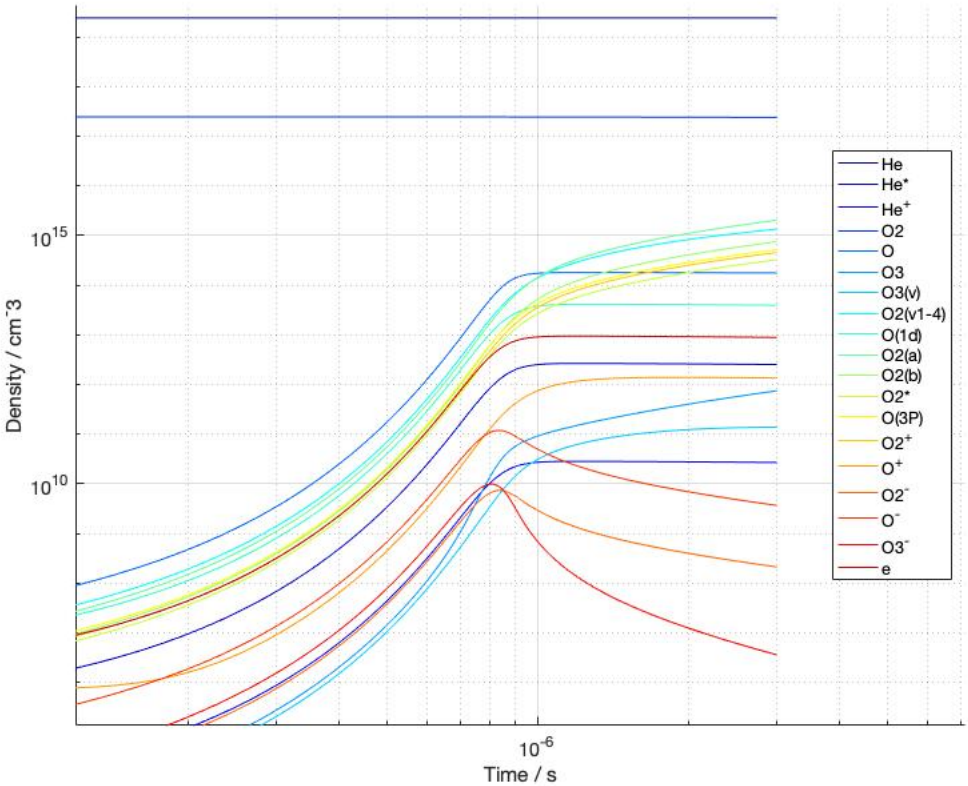

Figure 4.37 Species density evolution over time for an RF excited He:O2 0.99:0.01 mixture.

CHAPTER 5 CONCLUSION

This chapter concludes this work by briefly summarizing the thesis, identifying the limitations, and mentioning the next steps for this project.

5.1 Summary

To achieve better control over the generated species by atmospheric pressure plasma jets (APPJs), the work of this thesis was split into three parts. The first part was to develop a flexible, modular and scalable pulse high voltage power supply, the second was to recreate a $O_2(^1\Delta_g)$ emission spectroscopy in the effluent of such plasma, while the third was to establish a time-dependent reaction kinetics solver for plasma chemistry.

The high voltage pulsed power supply was designed and constructed into three stages. The first stage is comprised of the initial sinusoidal voltage generated by a waveform generator which is amplified by a broadband power amplifier, of 50 kHz bandwidth, before being isolated by a 1:1 isolation transformer and passed through a VARIAC to modulate the final amplitude of the pulse. The second stage is the Cockcroft-Walton (CW) generator, which takes this sinusoidal excitation, rectifies and amplifies it stage by stage to reach a high voltage DC. The final stage is the switching circuit. It encompasses the switch itself, the self-designed trigger circuit and the output circuit. The final stage switches on and off the high voltage from the CW generator, creating short pulses. For a purely resistive load of 72.3 kΩ, these pulse characteristics are obtained: 0-6 kV in amplitude, 500 Hz to 8 kHz repetition frequency, 1 μs to 10 μs FWHM with a 40 ns rise time. To test these pulses with air discharges, a simple DBD reactor was built. This tabletop reactor with round aluminum electrodes of 30 mm in diameter and a 50 mm diameter glass disk allowed plasma breakdown over a 0.5 mm air gap. The pulse characteristics for breakdown were the following: 6 kV in pulse amplitude, 2 kHz repetition frequency and 1 μs full width half maximum and 40 ns rise time.

In the $O_2(^1\Delta_g)$ measurements, a waveform generator, a broadband amplifier and a matching unit were used to power a capacitively coupled APPJ at 13.56 MHz. The effluent of this jet was collected and redirected by a glass adapter to a calibrated glass detection cell where NIR emission spectroscopy was performed. From the emitted light and measured voltage, absolute densities of $O_2(^1\Delta_g)$ were obtained by a conversion factor. Densities are measured

for different O_2 content in helium while the power, the measurement distance, and total flow are varied. Strong dependencies are observed for the total flow and measurement distance which comes down to time of flight before reaching the detection point hinting towards critical collisional quenching processes. For that reason, ozone densities were measured using the same setup but by changing the diagnostic to UV absorption.

Finally, the basic structure for a global model of plasma kinetics was established and validated with existing tools. A time-dependent Boltzmann equation solver was used to compute rate coefficients and other swarm parameters. An in-house chemistry solver which solves the evolution of different plasma species densities over time for a given set of conditions and gas mixture was also implemented. A graphical interface was created in the form of a MATLAB application to facilitate the use of this tool. The densities comparison of 2 examples from literature to our own calculations yielded very good agreement. Subsequently, a complex set of reactions in He:O_2 mixture was attempted to simulate the experimental conditions, but the kinetic reaction set will require further work to converge.

5.2 Limitations

Despite the strengths of these solutions, several limitations should be acknowledged. For the power supply, the present duration of the pulse is too long to have a true ns-pulse excitation. The intrinsic capacitance of the switch, causing this long trailing edge, is mentioned in the application notes of the switch and was expected. Also, the total current passing through the discharge is strongly limited by the CW generator, and some geometries of different reactors might have a too high current demand. Although the power supply is modular and part swapping is easy and inexpensive, a CW generator can never output a strong current and could limit the applications of this power supply for pulse applications.

As for the $O_2(^1\Delta_g)$ and O_3 detection setups, the power measurement's uncertainty has to be considered. In fact, the power measured by the bidirectional coupler placed between the broadband amplifier and the matching unit is a forward power. As the plasma conditions change, so does the impedance of the reactor and as a result, the matching unit circuit must be changed to maintain ideal matching. Because the control circuit of the matching unit was damaged, the variable capacitor matching values were kept constant. For that reason and to maintain constant applied power, the input voltage was adjusted at the arbitrary waveform generator. This power reading does not, however, truly represent the dissipated power by the plasma. It represents the power dissipated by the plasma plus the power dissipated in

the matching unit. A better way to measure power will be important, as it is the basis for comparisons. A good approach would be the one suggested in [38], where a coil was used to get better readings. Another limitation from the $O_2(^1\Delta_g)$ detection setup is the flow limit on the mass flows. The mass flow has a limit of 10 SLM, calibrated for hydrogen, which converts to 14.5 SLM for helium. Has seen in [27] high $O_2(^1\Delta_g)$ densities are observed with a higher flow, closer to 30 SLM. Collisional quenching of $O_2(^1\Delta_g)$ with ozone and NIR absorption of the 1270 nm photons by ozone in the detection cell is currently not taken into account in the Monte-Carlo ray-tracing simulation. Both factors induce an underestimation of the $O_2(^1\Delta_g)$ densities, but if $O_2(^1\Delta_g)$ is to be used in an application, collisional quenching would still occur.

On the reaction kinetics simulation side, only the chemistry in the plasma bulk, and not in the effluent of the plasma, is currently taken into account. The integration of the MATLAB Boltzmann equation solver inside a MATLAB chemistry solver was slower than established tools. Example 1 of ZDPlasKin takes around 10 s by the original tool and 45 s with the presented solution. The second example takes 50 s while our solution takes 3 min. Obtaining the densities over 10^{-4} s for the large He:O_2 model containing 108 reactions takes around 20 min on a basic desktop computer. A time-dependent solution is even slower to run. For example, obtaining the rate coefficients from Loki-B for a single ns-pulse of a very simple mixture takes about 2 min. While these computation times are not critical and can be further reduced, they should be acknowledged.

5.3 Future Research

In the near future, it is planned to implement the three components developed during this thesis into a system to control the chemical output of $O_2(^1\Delta_g)$ of plasma. Combining the developed high voltage power supply with the radio frequency generator will allow to generate pulse-sustained plasmas. To reach the full potential of pulse-sustained power, the pulse duration of the high voltage electric pulser will need to be shorter, which can be achieved simply by connecting a second switch between the high voltage pulse and the ground. To synchronize the two switches, the control circuit should be improved in precision, as the required two TTL signal timing control for the dual switch system would be more complex. Incorporation of all power supply components inside a box would improve general safety and transportability. Finally, a better way to determine the plasma dissipated power, as is currently being developed in the research group, is desirable.

On the simulation side, shorter computation should be investigated as well as the addition

of spatially-dependent plug-flow model. The plug-flow model would allow to simulate chemistry in the effluent and understand the quenching mechanisms and replicate the flow and measurement distance dependencies of the generated species densities. This work will lay the foundation for an electric-field-based control of the produced reactive species generated by atmospheric pressure plasmas.

REFERENCES

[1] Y. Liu, I. Korolov, J. Trieschmann, D. Steuer, V. Schulz-von der Gathen, M. Böke, L. Bischoff, G. Hübner, J. Schulze, and T. Mussenbrock, "Micro atmospheric pressure plasma jets excited in He/O2 by voltage waveform tailoring: a study based on a numerical hybrid model and experiments," *Plasma Sources Science and Technology*, vol. 30, no. 6, p. 064001, Jun. 2021. [Online]. Available: https://dx.doi.org/10.1088/1361-6595/abd0e0

[2] N. R. Council, *Plasma Science: Advancing Knowledge in the National Interest*. The National Academies Press, 2007. [Online]. Available: https://nap.nationalacademies.org/catalog/11960/plasma-science-advancing-knowledge-in-the-national-interest

[3] M. Radmilovic-Radjenovic, B. Radjenovic, M. Klas, A. Bojarov, and S. Matejcík, "The breakdown mechanisms in electrical discharges: The role of the field emission effect in direct current discharges in microgaps," *Acta Physica Slovaca*, vol. 63, pp. 105–205, 2013.

[4] G. Hagelaar, "Brief documentation of BOLSIG+ version 03/2016," vol. 118.

[5] T. Huiskamp, J. J. van Oorschot, M. T. Pereira, and L. M. Redondo, "Ozone Generation with a Flexible Solid-State Marx Generator," in *2018 IEEE International Power Modulator and High Voltage Conference (IPMHVC)*, Jun. 2018, pp. 147–150.

[6] Q. Yuan, S. Liu, G. Sun, H. Xue, W. Ding, Z. Wan, Y. Cheng, L. Ren, and Y. Wang, "A repetitive frequency square wave generator based on blumlein pulse forming network and pseudospark switch," vol. 95, no. 1, p. 014702. [Online]. Available: https://doi.org/10.1063/5.0186869

[7] T. Huiskamp, "Nanosecond pulsed streamer discharges Part I: Generation, source-plasma interaction and energy-efficiency optimization," *Plasma Sources Science and Technology*, vol. 29, no. 2, p. 023002, Feb. 2020. [Online]. Available: https://dx.doi.org/10.1088/1361-6595/ab53c5

[8] A. B. J. M. Driessen, E. J. M. van Heesch, T. Huiskamp, F. J. C. M. Beckers, and A. J. M. Pemen, "Compact pulse topology for adjustable high-voltage pulse generation using an sos diode," *IEEE Transactions on Plasma Science*, vol. 42, no. 10, pp. 3083–3088, 2014.

[9] K. Giotis, P. Svarnas, K. Petrou, M. Poupouzas, and D. K. Athanasopoulos, "Cockcroft–walton generator: An effective voltage multiplier for power supplies of square pulses driving DBD plasmas," vol. 50, no. 7, pp. 2185–2194.

[10] A. Mizuno, "Generation of non-thermal plasma combined with catalysts and their application in environmental technology," *Recent Advances in Plasma and Catalysis (ISPCEM 2012)*, vol. 211, pp. 2–8, Aug. 2013. [Online]. Available: https://www.sciencedirect.com/science/article/pii/S0920586113001314

[11] L. K. Randeniya and G. J. J. B. de Groot, "Non-Thermal Plasma Treatment of Agricultural Seeds for Stimulation of Germination, Removal of Surface Contamination and Other Benefits: A Review," *Plasma Processes and Polymers*, vol. 12, no. 7, pp. 608–623, Jul. 2015. [Online]. Available: https://doi.org/10.1002/ppap.201500042

[12] D. B. Graves, "Low temperature plasma biomedicine: A tutorial reviewa)," *Physics of Plasmas*, vol. 21, no. 8, p. 080901, Aug. 2014. [Online]. Available: https://doi.org/10.1063/1.4892534

[13] A. Fridman, "Introduction to Theoretical and Applied Plasma Chemistry," in *Plasma Chemistry*. Cambridge University Press, 2008, pp. 1–11. [Online]. Available: https://www.cambridge.org/core/books/plasma-chemistry/842EA140F5D8C59F15AB82544A3E44CC

[14] G. Bauer, D. Sersenová, D. B. Graves, and Z. Machala, "Cold atmospheric plasma and plasma-activated medium trigger RONS-based tumor cell apoptosis," vol. 9, no. 1, p. 14210. [Online]. Available: https://doi.org/10.1038/s41598-019-50291-0

[15] Y. Gao, K. Francis, and X. Zhang, "Review on formation of cold plasma activated water (PAW) and the applications in food and agriculture," vol. 157, p. 111246. [Online]. Available: https://www.sciencedirect.com/science/article/pii/S0963996922003039

[16] J. S. Sousa, K. Niemi, L. Cox, Q. T. Algwari, T. Gans, and D. O'connell, "Cold atmospheric pressure plasma jets as sources of singlet delta oxygen for biomedical applications," *Journal of Applied Physics*, vol. 109, no. 12, 2011.

[17] G. J. M. Hagelaar and L. C. Pitchford, "Solving the Boltzmann equation to obtain electron transport coefficients and rate coefficients for fluid models," *Plasma Sources Science and Technology*, vol. 14, no. 4, p. 722, Oct. 2005. [Online]. Available: https://dx.doi.org/10.1088/0963-0252/14/4/011

[18] S. Bekeschus and T. v. Woedtke, *Redox Biology in Plasma Medicine*, 1st ed. CRC Press, Jul. 2024. [Online]. Available: https://www.taylorfrancis.com/books/edit/10.1201/9781003328056/redox-biology-plasma-medicine-sander-bekeschus-thomas-von-woedtke

[19] M. Moisan, J. Barbeau, S. Moreau, J. Pelletier, M. Tabrizian, and L. Yahia, "Low-temperature sterilization using gas plasmas: a review of the experiments and an analysis of the inactivation mechanisms," *International Journal of Pharmaceutics*, vol. 226, no. 1, pp. 1–21, 2001. [Online]. Available: https://www.sciencedirect.com/science/article/pii/S0378517301007529

[20] J. Winter, J. S. Sousa, N. Sadeghi, A. Schmidt-Bleker, S. Reuter, and V. Puech, "The spatio-temporal distribution of he (23s1) metastable atoms in a mhz-driven helium plasma jet is influenced by the oxygen/nitrogen ratio of the surrounding atmosphere," *Plasma Sources Science and Technology*, vol. 24, no. 2, p. 025015, mar 2015. [Online]. Available: https://dx.doi.org/10.1088/0963-0252/24/2/025015

[21] H. Jablonowski, J. Santos Sousa, K.-D. Weltmann, K. Wende, and S. Reuter, "Quantification of the ozone and singlet delta oxygen produced in gas and liquid phases by a non-thermal atmospheric plasma with relevance for medical treatment," *Scientific Reports*, vol. 8, no. 1, p. 12195, Aug. 2018. [Online]. Available: https://doi.org/10.1038/s41598-018-30483-w

[22] N. Puač and N. Škoro, "Plasma–Liquid Interaction for Agriculture—A Focused Review," *Plasma Processes and Polymers*, vol. 22, no. 1, p. 2400208, Jan. 2025. [Online]. Available: https://doi.org/10.1002/ppap.202400208

[23] Y. Ju and W. Sun, "Plasma assisted combustion: Dynamics and chemistry," *Progress in Energy and Combustion Science*, vol. 48, pp. 21–83, Jun. 2015. [Online]. Available: https://www.sciencedirect.com/science/article/pii/S0360128514000781

[24] E. Skovsen, J. W. Snyder, and P. R. Ogilby, "Two-photon singlet oxygen microscopy: The challenges of working with single cells," *Photochemistry and Photobiology*, vol. 82, no. 5, pp. 1187–1197, 2006. [Online]. Available: https://onlinelibrary.wiley.com/doi/abs/10.1562/2006-04-10-IR-868

[25] S. Williams, M. Gupta, T. Owano, D. Baer, A. O'Keefe, and S. Matsika, "Quantitative detection of singlet O2 by cavity-enhanced absorption," *Optics Letters*, vol. 29, pp. 1066–1068, May 2004.

[26] Z. Kadhem, S. Alkafeef, and L. Benov, "Singlet oxygen detection in vivo is hindered by nonspecific SOSG staining," *Scientific Reports*, vol. 14, no. 1, p. 20669, Sep. 2024. [Online]. Available: https://doi.org/10.1038/s41598-024-71801-9

[27] J. S. Sousa, G. Bauville, B. Lacour, V. Puech, and M. Touzeau, "Atmospheric pressure generation of o2 (a1δg) by microplasmas," *The European Physical Journal-Applied Physics*, vol. 47, no. 2, p. 22807, 2009.

[28] S. Chur, R. Minke, Y. He, M. Vass, T. Mussenbrock, R. P. Brinkmann, E. Kemaneci, L. Schücke, V. S.-v. der Gathen, A. R. Gibson *et al.*, "Dynamics of reactive oxygen species produced by the cost microplasma jet," *arXiv preprint arXiv:2505.10204*, 2025.

[29] A. Hurlbatt, A. R. Gibson, S. Schröter, J. Bredin, A. P. S. Foote, P. Grondein, D. O'Connell, and T. Gans, "Concepts, capabilities, and limitations of global models: A review," *Plasma Processes and Polymers*, vol. 14, no. 1-2, p. 1600138, 2017.

[30] J. Stephens, "A multi-term Boltzmann equation benchmark of electron-argon cross-sections for use in low temperature plasma models," *Journal of Physics D: Applied Physics*, vol. 51, no. 12, p. 125203, Mar. 2018. [Online]. Available: https://dx.doi.org/10.1088/1361-6463/aaaf8b

[31] A. Tejero-del Caz, V. Guerra, D. Gonçalves, M. L. da Silva, L. Marques, N. Pinhão, C. D. Pintassilgo, and L. L. Alves, "The LisbOn KInetics Boltzmann solver," *Plasma Sources Science and Technology*, vol. 28, no. 4, p. 043001, Apr. 2019. [Online]. Available: https://dx.doi.org/10.1088/1361-6595/ab0537

[32] M. Rabie and C. Franck, "METHES: A Monte Carlo collision code for the simulation of electron transport in low temperature plasmas," *Computer Physics Communications*, vol. 203, pp. 268–277, Jun. 2016. [Online]. Available: https://www.sciencedirect.com/science/article/pii/S0010465516300376

[33] T. C. Dias, A. Tejero-del Caz, L. L. Alves, and V. Guerra, "The LisbOn KInetics Monte Carlo solver," *Computer Physics Communications*, vol. 282, p. 108554, Jan. 2023. [Online]. Available: https://www.sciencedirect.com/science/article/pii/S0010465522002739

[34] T. C. Dias and V. Guerra, "Are local-field and local-energy approximations appropriate for modeling nanosecond discharges?" *Journal of Physics D: Applied Physics*, vol. 58, no. 18, p. 185204, Apr. 2025. [Online]. Available: https://dx.doi.org/10.1088/1361-6463/adc277

[35] S. Pancheshnyi, B. Eismann, G. Hagelaar, and L. Pitchford, "ZDPlasKin: a new tool for plasmachemical simulations," *Bulletin of the American Physical Society*, vol. 53, 2008.

[36] X. Shao, D. A. Lacoste, and H. G. Im, "ChemPlasKin: A general-purpose program for unified gas and plasma kinetics simulations," *Applications in Energy and Combustion Science*, vol. 19, p. 100280, Sep. 2024. [Online]. Available: https://www.sciencedirect.com/science/article/pii/S2666352X24000359

[37] A. Ranjan, A. Abhishek, N. Kumar, and B. K. Verma, "Review of Nanosecond Pulse Generator With High-Power Switching Devices," *IEEE Transactions on Electron Devices*, vol. 71, no. 9, pp. 5165–5176, 2024.

[38] D. Filice and S. Coulombe, "Combined ns pulsed-RF excitation and impedance matching considerations for the production of moderate e/n atmospheric pressure discharges for gas conversion," vol. 33, no. 5, p. 055011. [Online]. Available: https://dx.doi.org/10.1088/1361-6595/ad42d0

[39] S. Reuter, *Formation Mechanisms of Atomic Oxygen in an Atmospheric Pressure Plasma Jet Characterised by Spectroscopic Methods.* Cuvillier Verlag, 2008. [Online]. Available: https://publications.polymtl.ca/43998/

APPENDIX A ELECTRICAL SCHEMATICS AND COMPONENTS

The control circuit schematic and PCB layout are presented in figure A.1 and A.2. The components used in this circuit and their respective cost are detailed in table A.2.

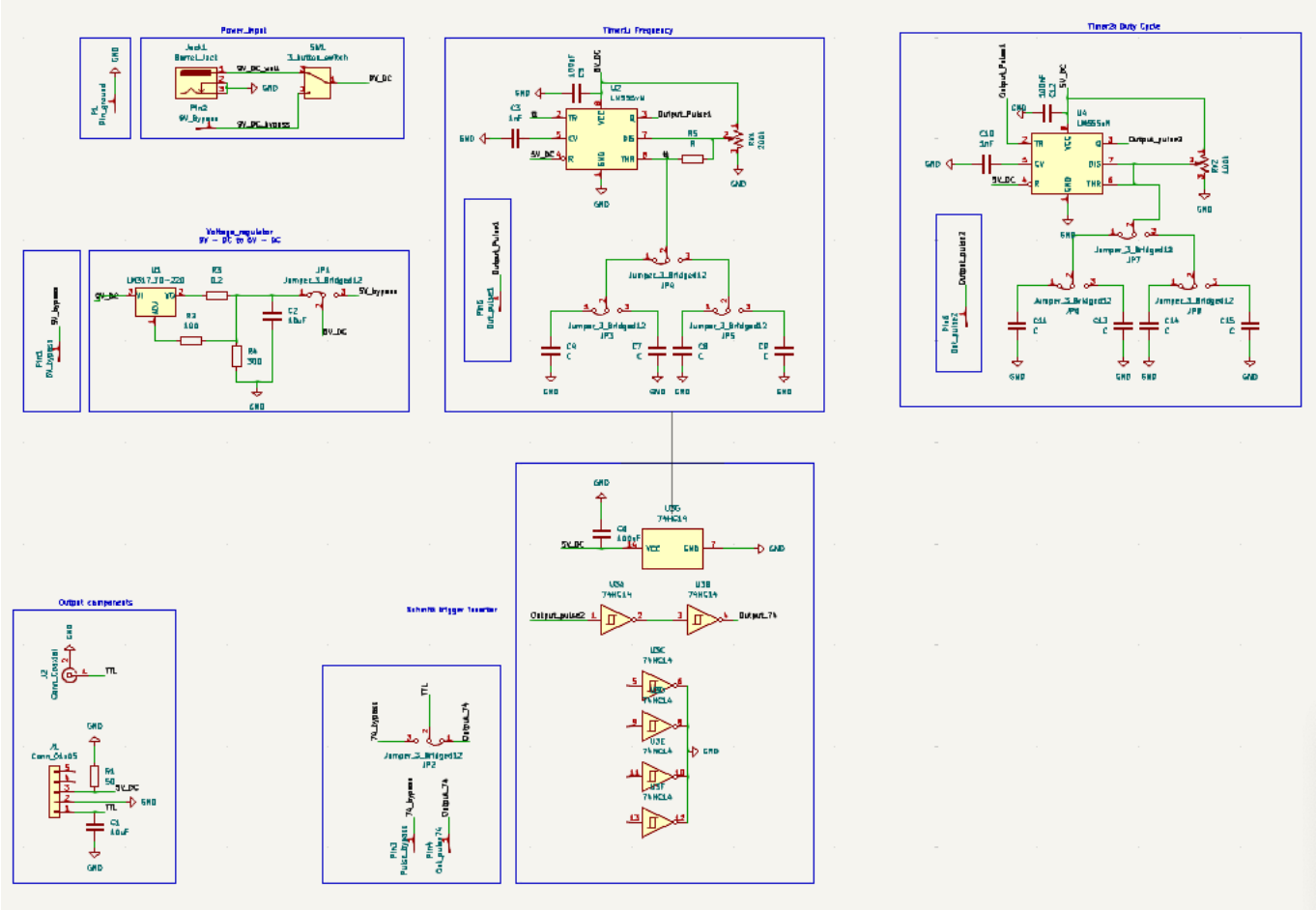

Figure A.1 BEHLKE switch control circuit schematic.

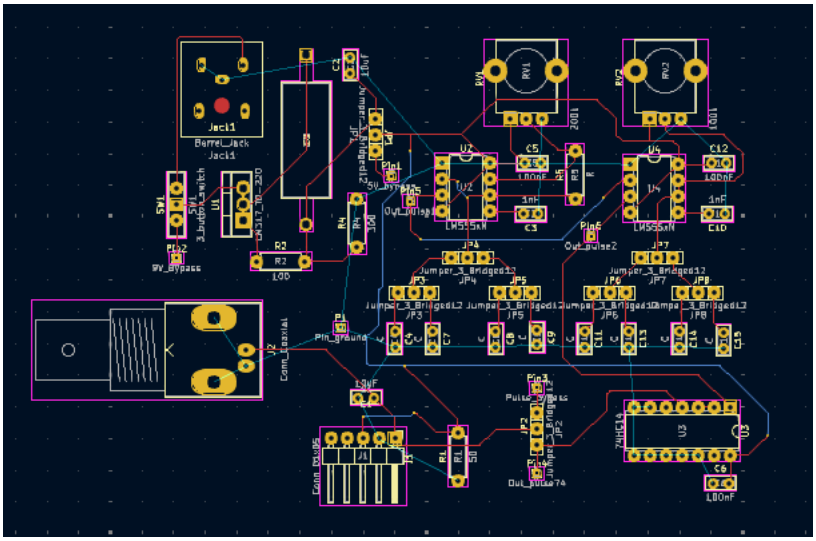

Figure A.2 BEHLKE switch control circuit PCB layout.

The components used for the 3 card CW generator are detailed in table A.1.

Table A.1 Components for the CW generator.

Component	Part number (Digikey	Value	Quantity	Price $
Capacitor	ESK226M400AL4AA	22 μF	60	1.019
Diode	UF5408-E3/54	-	60	0.58
PCB	-	-	3	≈10
				125.94

Table A.2 Components in the BEHLKE switch control circuit.

Component	**Part number (Digikey)**	**Value**	**Quantity**	**Price $**	**Link**
Pin 1x1	732-5314-ND	1 vertical position	7	0.19	link
Barrel Jack	CP-047AH-ND	-	1	1.45	link
Button switch	EG1903-ND	-	1	1.09	link
555 Timer	LMC555CN/NOPB-ND	-	2	2.53	link
Resistor	-	R1-55 ohm	1	0.15	-
Resistor	CF14JT100RCT-ND	R2 - 100 ohm	1	0.15	link
Resistor	749- AC05000002007JAC00CT-ND	R3 - 0.2 ohm	1	1.3	link
Resistor	CF14JT300RCT-ND	R4 - 326 ohm	1	0.15	link
Resistor	-	R5-1 ohm	1	0.15	-
Capacitor	399-4148-ND	C1,C2,C3,C10 - 10 uF	4	0.32	link
Capacitor	399-4148-ND	C5,C6,C12 - 100 nF	3	0.32	link
Capacitor	C320C102K3G5TA-ND	C4,C11 - 4700 pF	2	0.32	link
Capacitor	C320C102K3G5TA-ND	C7,C13 - 680 pF	2	0.32	link
Capacitor	C320C102K3G5TA-ND	C8,C9,C14,C15 -	4	0.32	link
Three pin jumper	732-5316-ND	1x3 pos vertical	8	0.19	link
Two pin connector	732-2678-ND	1x2 pos vertical	8	0.48	link
Five pin 90 degrees	732-5338-ND	-	1	0.62	link
BNC adapter	343-CONBNC002-ND	-	1	4.53	link
voltage regulator	LM317AT-ND	-	1	4.23	link
Schmitt trigger inverter	296-4301-5-ND	-	1	0.98	link
Potentiometer	PTV09A-4015F-B104-ND	100 kohm	1	1.49	link
Potentiometer	PTV09A-4030U-B204-ND	200 kohm	1	1.49	link

APPENDIX B PLASMA KINETICS

Table B.1 enumerates the chemical reactions taken into account for a He/O_2 gas mixture. The corresponding rates are in m^3/s or m^6/s for two-body and three-body reactions respectively. The gas temperature T_g is in K and the electron temperature T_e is in eV.

Table B.1 Reactions and corresponding rates for a He/O_2 plasma model [1].

Number	**Reaction**	**Rate**
1	e + He → e + He	$f(e)$
2	e + He → e + He(2^3S)	$f(e)$
3	e + He → e + He(2^1S)	$f(e)$
4	e + He → e + He(3^3S)	$f(e)$
5	e + He → e + e + He^+	$f(e)$
6	e + O_2 → e + O_2	$f(e)$
7	e + O_2 → O + O^-	$f(e)$
8	e + O_2 → e + O_2(v=1-4)	$f(e)$
9	e + O_2 → e + $O_2(a^1\Delta_g)$	$f(e)$
10	e + O_2 → e + $O_2(b^1\Sigma_g^+)$	$f(e)$
11	e + O_2 → e + O_2(4.05 eV)	$f(e)$
12	e + O_2 → e + O + O	$f(e)$
13	e + O_2 → e + O + O(^{1}D)	$f(e)$
14	e + O_2 → e + O(^{1}D) + O(^{1}D)	$f(e)$
15	e + O_2 → e + e + O_2^+	$f(e)$
16	e + O_2 → e + O + O(3p^3P)	$f(e)$
17	e + O_2 → e + e + O + O^+	$f(e)$
18	e + $2O_2$ → O_2 + O_2^-	$3.6 * 10^{-43} T_e^{-1} \exp(-\frac{0.052}{T_e})$
19	e + O_2^+ → O + O(^{1}D)	$9.1 * 10^{-15} T_e^{-0.7}$
20	O + O^- → e + O_2	$2.3 * 10^{-16} \left(\frac{300}{T_g}\right)^{1.3}$
21	O + O_2^- → O^- + O_2	$8.5 * 10^{-17} \left(\frac{300}{T_g}\right)^{1.8}$
22	O + O_2^- → e + O_3	$8.5 * 10^{-17} \left(\frac{300}{T_g}\right)^{1.8}$
23	O + O_3^- → e + $2O_2$	$1.0 * 10^{-17}$

Continued on next page

Table B.1 – *Continued from previous page*

Number	**Reaction**	**Rate**
24	$O + O_3^- \rightarrow O_2 + O_2^-$	$2.5 * 10^{-16}$
25	$O_2 + O^+ \rightarrow O + O_2^+$	$2.1 * 10^{-17} \left(\frac{300}{T_g}\right)^{0.4}$
26	$O^+ + O_3 \rightarrow O_2 + O_2^+$	$1.2 * 10^{-15}$
27	$O^- + O_2 \rightarrow e + O_3$	$1.0 * 10^{-18}$
28	$O^- + O_2 \rightarrow O + O_2^-$	$1.0 * 10^{-18}$
29	$O^- + 2O_2 \rightarrow O_2 + O_3^-$	$1.1 * 10^{-42}$
30	$O^- + O_2(a^1\Delta_g) \rightarrow O + O_2^-$	$7.9 * 10^{-16} \exp(-\frac{890}{T_g})$
31	$O^- + O_2(a^1\Delta_g) \rightarrow e + O_3$	$6.1 * 10^{-17}$
32	$O^- + O_2(b^1\Sigma_g^+) \rightarrow O + O_2^-$	$7.9 * 10^{-16} \exp(-\frac{890}{T_g})$
33	$O^- + O_2(b^1\Sigma_g^+) \rightarrow e + O_3$	$6.1 * 10^{-17}$
34	$O^- + O_2^+ \rightarrow 3O$	$1.61 * 10^{-14} \left(\frac{300}{T_g}\right)^{1.1}$
35	$O^- + O_2^+ \rightarrow O + O_2$	$1.61 * 10^{-14} \left(\frac{300}{T_g}\right)^{1.1}$
36	$O^- + O_3 \rightarrow e + 2O_2$	$3.0 * 10^{-16}$
37	$O^- + O_3 \rightarrow O + O_3^-$	$2.0 * 10^{-16}$
38	$O^- + O_3 \rightarrow O_2 + O_2^-$	$1.0 * 10^{-17}$
39	$O_2(a^1\Delta_g) + O_2^- \rightarrow e + 2O_2$	$7.0 * 10^{-16}$
40	$O_2(b^1\Sigma_g^+) + O_2^- \rightarrow e + 2O_2$	$7.0 * 10^{-16}$
41	$O_2(b^1\Sigma_g^+) + O_3^- \rightarrow O^- + 2O_2$	$6.7 * 10^{-16} \exp(-\frac{1300}{T_g})$
42	$O_2^+ + O^- + O_2 \rightarrow O + 2O_2$	$1.0 * 10^{-37} \left(\frac{300}{T_g}\right)^{2.5}$
43	$O_2^+ + O^- + O_2 \rightarrow O_2 + O_3$	$1.0 * 10^{-37} \left(\frac{300}{T_g}\right)^{2.5}$
44	$O_2^+ + O_2^- + O_2 \rightarrow 3O_2$	$2.0 * 10^{-37} \left(\frac{300}{T_g}\right)^{2.5}$
45	$O_2^+ + O_3^- + O_2 \rightarrow 2O_2 + O_3$	$2.0 * 10^{-37} \left(\frac{300}{T_g}\right)^{2.5}$
46	$O_2^+ + O_2^- \rightarrow O_2 + 2O$	$1.6 * 10^{-14} \left(\frac{300}{T_g}\right)^{1.1}$
47	$O_2^+ + O_2^- \rightarrow 2O_2$	$1.6 * 10^{-14} \left(\frac{300}{T_g}\right)^{1.1}$
48	$O_2^+ + O_3^- \rightarrow O_3 + 2O$	$2.9 * 10^{-14} \left(\frac{300}{T_g}\right)^{0.9}$
49	$O_2^+ + O_2^- \rightarrow O_2 + O_3$	$2.9 * 10^{-14} \left(\frac{300}{T_g}\right)^{0.9}$
50	$O_2^- + O_3 \rightarrow O_2 + O_3^-$	$6.0 * 10^{-16}$
51	$O_3^- + O_3 \rightarrow e + 3O_2$	$8.5 * 10^{-16}$
52	$3O \rightarrow O + O_2$	$3.8 * 10^{-44} (\frac{300}{T_g}) \exp(-\frac{170}{T_g})$
53	$3O \rightarrow O + O_2(b^1\Sigma_g^+)$	$1.4 * 10^{-42} \exp(-\frac{650}{T_g})$
54	$2O + O_2 \rightarrow O + O_3$	$4.2 * 10^{-47} \exp(-\frac{1056}{T_g})$

Continued on next page

Table B.1 – *Continued from previous page*

Number	**Reaction**	**Rate**
55	$2O + O_2 \rightarrow O + O_3(v)$	$9.8 * 10^{-47} \exp(-\frac{1056}{T_g})$
56	$2O + O_2 \rightarrow O_2(a^1\Delta_g) + O_2$	$6.5 * 10^{-45}(\frac{300}{T_g}) \exp(-\frac{170}{T_g})$
57	$2O + O_2 \rightarrow O_2(b^1\Sigma_g) + O_2$	$6.5 * 10^{-45}(\frac{300}{T_g}) \exp(-\frac{170}{T_g})$
58	$O + O(^1D) \rightarrow 2O$	$2.8 * 10^{-18}$
59	$O + 2O_2 \rightarrow O_2 + O_3$	$1.8 * 10^{-46}(\frac{300}{T_g})^{2.6}$
60	$O + 2O_2 \rightarrow O_2 + O_3(v)$	$4.2 * 10^{-46}(\frac{300}{T_g})^{2.6}$
61	$O + O_2 + O_2(a^1\Delta_g) \rightarrow O + 2O_2$	$1.1 * 10^{-44}$
62	$O + O_2 + O_3 \rightarrow O_3 + O_3(v)$	$3.27 * 10^{-47} \exp(-\frac{1050}{T_g})$
63	$O + O_2(a^1\Delta_g) \rightarrow O + O_2$	$1.0 * 10^{-22}$
64	$O + O_2(b^1\Sigma_g^+) \rightarrow O + O_2(a^1\Delta_g)$	$8.0 * 10^{-20}$
65	$O + O_3 \rightarrow 2O_2(v=1\text{-}4)$	$8.0 * 10^{-18} \exp(-\frac{2060}{T_g})$
66	$O + O_3(v) \rightarrow 2O_2$	$4.5 * 10^{-18}$
67	$O + O_3(v) \rightarrow O_3 + O$	$1.05 * 10^{-17}$
68	$O(^1D) + O_2 \rightarrow O + O_2(b^1\Sigma_g^+)$	$2.64 * 10^{-17} \exp(\frac{55}{T_g})$
69	$O(^1D) + O_2 \rightarrow O + O_2(a^1\Delta_g)$	$6.6 * 10^{-18} \exp(\frac{55}{T_g})$
70	$O(^1D) + O_3 \rightarrow 2O + O_2$	$1.2 * 10^{-16}$
71	$O(^1D) + O_3 \rightarrow 2O_2$	$1.2 * 10^{-16}$
72	$O_2 + O_2(v=1\text{-}4) \rightarrow 2O_2$	$2.0 * 10^{-20}$
73	$O_2 + O_2(a^1\Delta_g) \rightarrow 2O_2$	$3.6 * 10^{-26} \exp(-\frac{220}{T_g})$
74	$O_2 + O_2(b^1\Sigma_g^+) \rightarrow O_2 + O_2(a^1\Delta_g)$	$3.9 * 10^{-23}$
75	$O_2 + O_3(v) \rightarrow O_2 + O_3$	$4.0 * 10^{-20}$
76	$O_2(a^1\Delta_g) + O_3 \rightarrow O + 2O_2$	$5.2 * 10^{-17} \exp(-\frac{2840}{T_g})$
77	$O_2(a^1\Delta_g) + O_3(v) \rightarrow O_2 + O_3$	$5.0 * 10^{-17}$
78	$O_2(b^1\Sigma_g^+) + O_3 \rightarrow O + 2O_2$	$2.4 * 10^{-17} \exp(-\frac{135}{T_g})$
79	$O_2(b^1\Sigma_g^+) + O_3 \rightarrow O_2 + O_3$	$5.5 * 10^{-18} \exp(-\frac{135}{T_g})$
80	$O_2(b^1\Sigma_g^+) + O_3 \rightarrow O_2(a^1\Delta_g) + O_3$	$2.4 * 10^{-17} \exp(-\frac{135}{T_g})$
81	$O_3 + O_3(v) \rightarrow 2O_3$	$1.9 * 10^{-19}$
82	$e + He + O_2 \rightarrow He + O_2^-$	$1.0 * 10^{-44} T_e^{-0.5}$
83	$He + O^- + O_2 \rightarrow He + O_3^-$	$3.7 * 10^{-43}(\frac{300}{T_g})$
84	$He + O^- + O_2^+ \rightarrow He + O + O_2$	$2.0 * 10^{-37}(\frac{300}{T_g})^{2.5}$
85	$He + O_2^- + O_2^+ \rightarrow He + 2O_2$	$2.0 * 10^{-37}(\frac{300}{T_g})^{2.5}$

Continued on next page

Table B.1 – *Continued from previous page*

Number	**Reaction**	**Rate**
86	$He + O_3^- + O_2^+ \rightarrow He + O_2 + O_3$	$2.0 * 10^{-37}(\frac{300}{T_g})^{2.5}$
87	$He^+ + O \rightarrow He + O^+$	$5.8 * 10^{-16}$
88	$He^+ + O_2 \rightarrow He + O + O^+$	$9.7 * 10^{-16}$
89	$He^+ + O_2 \rightarrow He + O_2^+$	$3.0 * 10^{-17}$
90	$He^+ + O_2(a^1\Delta_g) \rightarrow He + O + O^+$	$9.7 * 10^{-16}$
91	$He^+ + O_2(b^1\Sigma_g^+) \rightarrow He + O + O^+$	$9.7 * 10^{-16}$
92	$He^+ + O_3 \rightarrow He + O_2 + O^+$	$2.2 * 10^{-15}$
93	$He^+ + He^* + O_2 \rightarrow e + 2He + O_2^+$	$1.6 * 10^{-43}$
94	$He + 2O \rightarrow He + O_2(a^1\Delta_g)$	$2.0 * 10^{-45}(\frac{300}{T_g})\exp(-\frac{170}{T_g})$
95	$He + 2O \rightarrow He + O_2(b^1\Sigma_g^+)$	$2.0 * 10^{-45}(\frac{300}{T_g})\exp(-\frac{170}{T_g})$
96	$He + O + O_2 \rightarrow He + O_3$	$9.0 * 10^{-47}(\frac{300}{T_g})^{2.6}$
97	$He + O + O_2 \rightarrow He + O_3(v)$	$2.1 * 10^{-46}(\frac{300}{T_g})^{2.6}$
98	$He + O + O_2(a^1\Delta_g) \rightarrow He + O + O_2$	$4.5 * 10^{-45}$
99	$He + O(^1D) \rightarrow He + O$	$1.0 * 10^{-21}$
100	$He + O_2(v=1\text{-}4) \rightarrow He + O_2$	$1.0 * 10^{-20}(\frac{300}{T_g})^{-0.5}$
101	$He + O_2(a^1\Delta_g) \rightarrow He + O_2$	$5.0 * 10^{-27}$
102	$He + O_2(b^1\Sigma_g^+) \rightarrow He + O_2(a^1\Delta_g)$	$4.3 * 10^{-24}$
103	$He + O_3(v) \rightarrow He + O_3$	$6.0 * 10^{-20}$
104	$He^* + O \rightarrow e + He + O^+$	$2.6 * 10^{-16}$
105	$He^* + O_2 \rightarrow e + He + O_2^+$	$2.6 * 10^{-16}$
106	$He^* + O_2(a^1\Delta_g) \rightarrow e + He + O_2^+$	$2.6 * 10^{-16}$
107	$He^* + O_2(b^1\Sigma_g^+) \rightarrow e + He + O_2^+$	$2.6 * 10^{-16}$
108	$He^* + O_3 \rightarrow e + He + O + O_2^+$	$2.6 * 10^{-16}$